Unnamed Systems, Vol. 14, No. 4 (2026) 731–748

DOI: 10.1142/S2301385026500159

Unmanned Systems
https://www.worldscientific.com/worldscinet/us

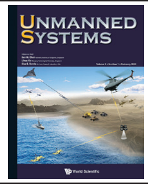

Precise Dynamic Modeling and Control of a Net-Throwing Aerial Vehicle in Capturing Flying Objects

Mirshams Baha*, Fariborz Saghafi†

Department of Aerospace Engineering,
Sharif University of Technology,
P.O. Box 11365-11155, Tehran, Iran

The purpose of this paper is to provide a comprehensive mathematical model and control strategy for a Net-Throwing Aerial Vehicle (NTAV) to grab flying objects with high reliability. To achieve this goal, by describing the flight phases of the mission and the overall dynamics of flying objects, the process of extracting equations of motion is expressed in tensor form. Then, a control strategy for this multi-step mission is introduced. Due to the nonlinear nature of the aerial vehicle and the presence of intense time-varying loads and uncertainties after capturing the unknown target, a robust control system based on generalized super-twisting sliding mode control (GSTSMC) approach is designed for this under-actuated system. The controller is able to estimate the target inertia precisely, which effectively leads to a reduction of tracking error without deteriorating transient response. In this regard, the performance of the designed controller compared with the generalized and super-twisting sliding mode controllers (GSMC and STSMC) is evaluated based on some standard metrics such as integral absolute error and control input. The results show the validity of the proposed model and the desired performance of the control system without expending more control effort.

Keywords: Dynamic modeling; NTAV; multi-step mission; flying objects; GSTSMC; parameter estimation.

1. Introduction

In the last two decades, unmanned aerial vehicles (UAVs), due to their diversity, relative low cost and wide range of applications, especially their ability to operate in a dense environment, have attracted a large segment of scientific researchers in various fields of engineering [1–5]. One of the most interesting topics in this area is the design and development of an aerial robot with the ability to grasp and transport objects [6, 7]. This issue becomes more challenging when it is decided to use these vehicles to capture flying objects with high maneuverability. The subject that is a hot topic among researchers.

In recent years, the main focus has been on designing and developing flying robots equipped with a manipulator to achieve a system with the ability to grasp, transport and deploy objects. These studies can be classified into two categories. In the first one, the concentration of researchers such as Mellinger *et al.* [8], Kim *et al.* [9], Khalifa and Fanni [10], Suarez *et al.* [11], Emami and Banazadeh [12] and Yang *et al.* [13] has been on developing aerial manipulators to pick up a stationary object in hovering phase and then transport it to a destination point, either individually or cooperatively. In this regard, parallel to structural development (no arm, single arm and multi-arm), it has been tried to improve the capabilities of the system during grasping and transporting the object from stability, robustness and tracking point of views, employing different control strategies. The second category, which is a more challenging subject, is the studies in which the researchers tried to achieve avian-inspired robots with the ability to grab an object in high-speed flight. In an innovative work, Thomas *et al.* designed, modeled and controlled a hunting quadrotor through investigating the motion of birds of prey [14, 15]. Based on this study, Song and Hu, developed an adaptive MPC for a hunting system in order to achieve the

Received 28 February 2024; Accepted 8 February 2025; Published 28 March 2025. This paper was recommended for publication in its revised form by editorial board member, Hailong Pei.
Email Addresses: **baha.mirshams@ae.sharif.ir*, †*saghafi@sharif.edu*
†Corresponding author.

goal of precise tracking of a nominal trajectory [16]. In another study, Stewart *et al.* presented a fixed-wing UAV equipped with a manipulator for high-speed grasping [17].

Although the gripper-based aerial robots have the advantages of firm grasping and accurate transporting and positioning, it is very difficult to apply them for capturing flying objects due to the small contact surface of the end effector, and if realized, it leads to a very expensive system. On the other hand, flying targets have significant inertia and active dynamics, which, due to the integrated nature of the manipulator-vehicle systems, can strongly affect their dynamics, leading to instability and collapse of the control system. In this respect, some researchers have tried to solve this problem via applying a soft manipulator mechanism. Fishman and Carlone studied minimum snap trajectory optimization and geometric control for an aerial vehicle equipped with a soft manipulator [18]. In another research, Appius *et al.* equipped a quadrotor with a Fin Rey manipulator to enhance the capability of the flying system in rapid grasping and transporting [19]. Although these studies have tried to enhance the chance of the operation success through increasing the contact surface and flexibility of the manipulator, capturing flying objects by these aerial robots is still difficult due to the control complexity. Hence, achieving a system capable of capturing flying objects is very challenging issue. This study has intended to address this problem and tried to solve it to some extent.

The reliability of the capturing process and the safety issues associated with transporting noncooperative moving targets have led this research to present a new method of capturing and transporting that involves using a net-cable system. Although [20] has somehow studied a similar topic, the main purpose of that research is the vision-based detection and interception of another small UAV, and not precise multi-step modeling and robust control, especially after capturing an unknown flying object. Also, its net-launch mechanism is different. In this study, a net-cable that is initially accommodated in the air vehicle body is thrown toward the target and after capturing, it is transported like a cable-payload transportation system [21–23]. This vehicle facilitated by this system is named as NTAV. Having replaced the gripper by a net, the air vehicle agility in the pursuit phase and the probability of capturing success are greatly increased, and at the same time, the impact of the target on attitude of the aerial vehicle is significantly reduced due to the single point connection of the cable-target set. However, a new challenge of destabilizing effect of the cable impulsive force exerted by the target during capturing process arises, which needs to be carefully treated.

Regarding the fact that at the moment of capturing a high-weight moving object, the dynamics of the flying system is substantially affected by intense uncertainties including disturbances and impulsive forces and moments, a highly efficient control system based on GSTSMC approach is designed for this MIMO under-actuated system. The controller is equipped with an estimator to identify target's mass precisely, which significantly improves tracking performance and reduces control effort, especially at the moment of grabbing the target. In this regard, the stability of the closed-loop system is proved via the Lyapunov theory. At the end, the performance of the presented controller in comparison with GSMC and STSMC is evaluated through numerical simulation.

The contributions of this study can be summarized as follows:

(1) Precise multi-step modeling of the new concept of a Net-Throwing Aerial Vehicle in capturing flying objects.
(2) Designing a high performance robust control system for a flying robot in a specific mission of net-throwing capturing based on GSTSMC approach that involves an accurate target mass estimation process.
(3) Evaluating the efficiency of the designed controller compared with two other robust controllers based on some standard metrics.

The rest of the paper proceeds as follows: In Sec. 2: a precise hybrid mathematical model of the system is derived. In Sec. 3: the control strategy is expressed and an adaptive model-based robust nonlinear control system is designed for the aerial vehicle. In Sec. 4: numerical simulation is performed to show the efficiency and robustness of the designed controller in comparison with the two other advanced robust nonlinear controllers. Finally, concluding remark is discussed in Sec. 5.

2. Dynamic Modeling

In this section, the mission's phases are described and the process of modeling is expressed in tensor form [24]. In this respect, m_i indicates the mass of component i, $\boldsymbol{I}_k^k$ is the inertia tensor of the body k referred to the point k, $\boldsymbol{s}_{ik}$ shows the displacement vector of the point i with respect to the point k and $\boldsymbol{v}_i^k$ and $\boldsymbol{\omega}^{ik}$ represent the velocity of the point i with respect to the frame k and the angular velocity of the frame i with respect to the frame k, respectively. Also, $\boldsymbol{S}_{ik}$ and $\boldsymbol{\Omega}^{ik}$ are the skew symmetric matrices of $\boldsymbol{s}_{ik}$ and $\boldsymbol{\omega}^{ik}$, respectively. An important mathematical operator to extract the equations of motion is the rotational time derivative of the vector * with respect to the frame k which is indicated as $D^k(*)$. Here, i and k are dummy indices and in this case are replaced by specific points or frames. In Fig. 1 (a), NTAV at the moment of capturing a flying object is shown.

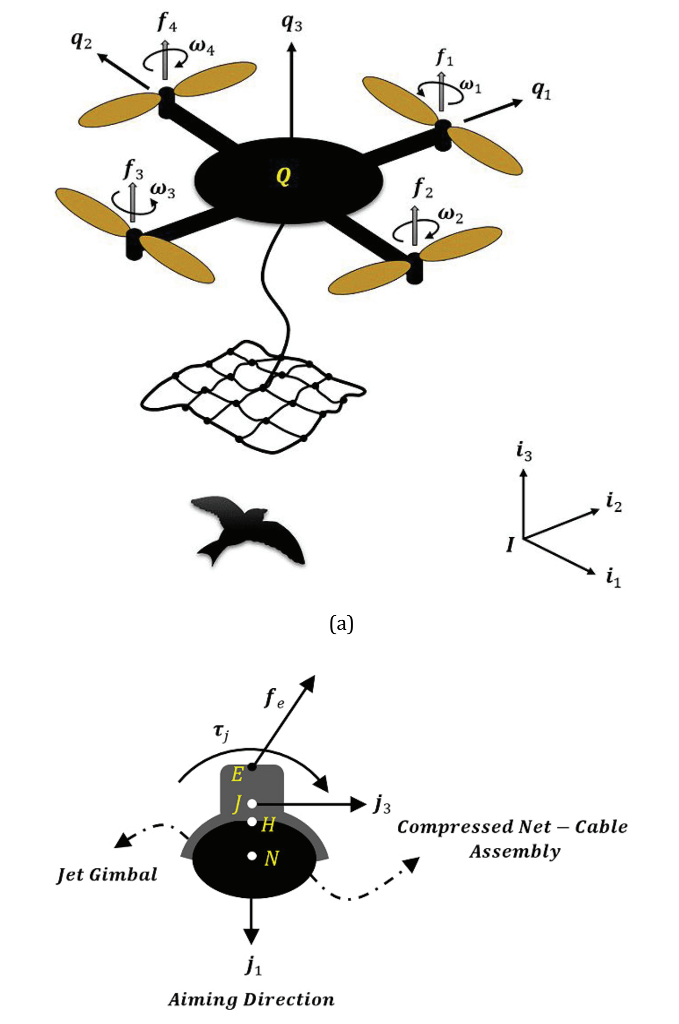

(a)

(b)

Fig. 1. (a) NTAV at the moment of capturing a flying object and (b) Magnified view of jet-net-cable assembly.

2.1. *Pursuit phase*

In the pursuit phase, the flying vehicle can be considered as a 2-body system: 1. Quadrotor and 2. Jet-net-cable assembly, in which the jet is the net-throwing mechanism.

Assumption 1. The flying vehicle has a plus configuration with symmetric mass distribution.

Assumption 2. The net-cable set is in the form of a rigid body connected to the jet as depicted in Fig. 1(b).

The inertial ($\boldsymbol{I}$), quadrotor body ($\boldsymbol{Q}$) and jet body ($\boldsymbol{J}$) frames are considered according to Fig. 1. In this respect, Q, E, H, J and N represent the c.g of the quadrotor, connection points of the jet to the vehicle and the cable to the jet, the c.g of the jet and compressed net-cable set, respectively. The aiming direction of the jet, shown in Fig. 1(b), with respect to the quadrotor is determined by two angles γ and χ, in which γ shows the rotation around $\boldsymbol{q}_3$ and χ indicates the orientation angle of $\boldsymbol{j}_1$ with respect to $-\boldsymbol{q}_3$. Therefore, the system state variables in this phase are as (x, y, z), (ϕ, θ, ψ) and (χ, γ), which define the position of the quadrotor in inertial coordinate system and the bodies' Euler angles, respectively.

The transformation matrix and angular velocity of jet body frame are expressed in Appendix A.

The kinetic equations of the quadrotor subsystem through Newton–Euler law are obtained as

$$m_Q D^I \boldsymbol{v}_Q^I = \boldsymbol{f} + \boldsymbol{f}_e + \boldsymbol{f}_{a_q} + m_Q \boldsymbol{g}, \tag{1}$$

$$D^Q(\boldsymbol{I}_Q^Q \boldsymbol{\omega}^{QI}) + \boldsymbol{\Omega}^{QI}(\boldsymbol{I}_Q^Q \boldsymbol{\omega}^{QI}) = \boldsymbol{\tau} + \boldsymbol{\tau}_j + \boldsymbol{S}_{EQ}\boldsymbol{f}_e + \boldsymbol{\tau}_{gyr}, \tag{2}$$

and for jet-net-cable assembly, one gets

$$m_J D^I \boldsymbol{v}_J^I + m_N D^I \boldsymbol{v}_N^I = \boldsymbol{f}_e + (m_J + m_N)\boldsymbol{g}, \tag{3}$$

$$\begin{aligned} D^J(\boldsymbol{I}_J^J \boldsymbol{\omega}^{JI}) &+ \boldsymbol{\Omega}^{JI}(\boldsymbol{I}_J^J \boldsymbol{\omega}^{JI}) + D^N(\boldsymbol{I}_N^N \boldsymbol{\omega}^{NI}) \\ &+ \boldsymbol{\Omega}^{NI}(\boldsymbol{I}_N^N \boldsymbol{\omega}^{NI}) + m_J \boldsymbol{S}_{JE} D^I \boldsymbol{v}_J^I + m_N \boldsymbol{S}_{NE} D^I \boldsymbol{v}_N^I \\ &= \boldsymbol{\tau}_j + \boldsymbol{\tau}_{d_j} + m_J \boldsymbol{S}_{JE}\boldsymbol{g} + m_N \boldsymbol{S}_{NE}\boldsymbol{g}, \end{aligned} \tag{4}$$

where $\boldsymbol{\omega}^{NI} = \boldsymbol{\omega}^{JI}$ based on Assumption 2. In the above relations, $\boldsymbol{g}$ is the gravitational acceleration, $\boldsymbol{f}$ and $\boldsymbol{\tau}$ are the vectors of force and torque produced by the vehicle's rotors, $\boldsymbol{f}_e$ is the internal force at the connection point E, $\boldsymbol{\tau}_j$ is the jet servo's torque and $\boldsymbol{f}_{a_q}$, $\boldsymbol{\tau}_{d_j}$ and $\boldsymbol{\tau}_{gyr}$ denote the drag force on the quadrotor, dissipative moment at the connection point of jet to the vehicle and gyroscopic moment, respectively, which are obtained as follows:

$$\boldsymbol{f}_{a_q} = -\frac{1}{2}\rho A_Q \boldsymbol{C}_{D_Q} \boldsymbol{v}_Q^I \cdot |\boldsymbol{v}_Q^I|, \tag{5}$$

$$\boldsymbol{\tau}_{d_j} = -C_{d_j} \boldsymbol{\omega}^{JQ}, \tag{6}$$

$$\boldsymbol{\tau}_{gyr} = J_r \boldsymbol{\Omega}^{QI} \begin{bmatrix} 0 & 0 & \sum_\omega \end{bmatrix}^T; \quad \sum_\omega = \sum (-1)^i \omega_i, \tag{7}$$

where ρ is the air density, A_Q is the reference area and $\boldsymbol{C}_{D_Q} = \mathrm{diag}([C_{D_{q_1}} \ C_{D_{q_2}} \ C_{D_{q_3}}])$ is the diagonal matrix of the drag coefficients, corresponding to the directions of the quadrotor body frame axes. Also, C_{d_j} indicates the dissipative coefficient, and J_r and ω_i are the inertia moment and angular speed of rotor i.

Assumption 3. Since the aerodynamic center of the multirotor platform is very close to the c.g of the vehicle, it is assumed that the moment generated by drag force is negligible [25].

2.2. *Capturing phase*

Having assumed that the net-throwing is abruptly executed, this phase is divided into two parts: 1. The approach and throwing net toward the target, in which the dynamics of the quadrotor is affected by the impulse of the net-cable assembly. 2. At the moment of complete opening of the net-cable set in which due to the different velocities of the quadrotor and the trapped target, another impulse is applied to the aerial vehicle.

Assumption 4. Inspired by a web shooting spider, the net has high adhesion and is completely opened before contacting the target as shown in Fig. 1(a) [26].

Assumption 5. The trapped target is considered as a point mass which generates quasi-stochastic forces.

Equations (1) and (2) prevail at the moment of shooting, but taking into consideration the fact that the impulsive force $\boldsymbol{f}_{\delta_n}$ is in alignment with the aiming direction that passes through the c.g and the connection point of the jet to the quadrotor, Eqs. (3) and (4) are changed as follows:

$$m_J D^I \boldsymbol{v}_J^I = \boldsymbol{f}_e + \boldsymbol{f}_{\delta_n} + m_J \boldsymbol{g}, \tag{8}$$

$$D^J(\boldsymbol{I}_J^J \boldsymbol{\omega}^{JI}) + \boldsymbol{\Omega}^{JI}(\boldsymbol{I}_J^J \boldsymbol{\omega}^{JI}) + m_J \boldsymbol{S}_{JE} D^I \boldsymbol{v}_J^I = \boldsymbol{\tau}_j + \boldsymbol{\tau}_{d_j} + m_J \boldsymbol{S}_{JE} \boldsymbol{g}, \tag{9}$$

with

$$\boldsymbol{f}_{\delta_n} = \begin{cases} \dfrac{m_N \boldsymbol{v}_N^J}{\Delta t} & t_s \le t < t_s + \Delta t, \\ 0 & \text{else}, \end{cases} \tag{10}$$

where t_s, $\boldsymbol{v}_N^J$ and Δt indicate the shooting time, lunch velocity of net-cable set with respect to the jet and shooting interval, respectively. The translational equation of the net-cable assembly before hitting the target is

$$m_N D^I \boldsymbol{v}_N^I = \boldsymbol{f}_{\delta_n} + \boldsymbol{f}_{a_n} + m_N \boldsymbol{g}, \tag{11}$$

where, $\boldsymbol{f}_{a_n}$ represents the drag force on the net-cable assembly, which is formulated as relation (5) with A_N, $\boldsymbol{C}_{D_N}$ and $\boldsymbol{v}_N^I$.

Assumption 6. Considering a very short time interval of throwing, opening and hitting the target that involves rapid net spreading and changes in drag force, an average aerodynamic drag coefficients $\boldsymbol{C}_{D_N} = \text{diag}([C_{D_{n_1}} \; C_{D_{n_2}} \; C_{D_{n_3}}])$ and reference area A_N are considered for this set during this period.

The speed of the target just after being trapped is obtained from the conservation of linear momentum as follows:

$$\boldsymbol{v}_T^I = \frac{m_N \boldsymbol{v}_N^I + m_{T_r} \boldsymbol{v}_{T_r}^I}{m_N + m_{Tr}}, \tag{12}$$

where m_{T_r} and $\boldsymbol{v}_{T_r}^I$ are the mass and velocity of the flying target.

The motion of the net-target set as a free flight object in the short time interval between the net hitting the target and the complete opening of the cable is governed by the following equation:

$$m_T D^I \boldsymbol{v}_T^I = \boldsymbol{f}_{a_t} + m_T \boldsymbol{g}, \tag{13}$$

where m_T indicates the mass of the trapped target (net plus target) and $\boldsymbol{f}_{a_t}$ is the aerodynamic drag force on this set which its detailed formulation is expressed in the next section.

In the second part, the velocity of the vehicle and the target at the moment before and after the engagement in the cable's direction, Fig. 2(a), are related to each other as follows [27]:

$$m_T(\boldsymbol{v}_{T_2}^I - \boldsymbol{v}_{T_1}^I) \cdot \boldsymbol{c}_1 = -\delta, \tag{14}$$

$$(m_Q + m_J)(\boldsymbol{v}_{Q_{J_2}}^I - \boldsymbol{v}_{Q_{J_1}}^I) \cdot \boldsymbol{c}_1 = \delta. \tag{15}$$

In the above relations, $\boldsymbol{v}_{Q_J}^I$ is the instantaneous velocity of the c.g of quadrotor-jet assembly, Q_J, and indices 1 and 2 indicate the conditions before and after the collision, respectively. Also, δ is the impulse caused by the collision. The relative speed of these two points are related to each other through the following equation:

$$e = \frac{(\boldsymbol{v}_{Q_{J_2}}^I - \boldsymbol{v}_{T_2}^I) \cdot \boldsymbol{c}_1}{(\boldsymbol{v}_{T_1}^I - \boldsymbol{v}_{Q_{J_1}}^I) \cdot \boldsymbol{c}_1}, \tag{16}$$

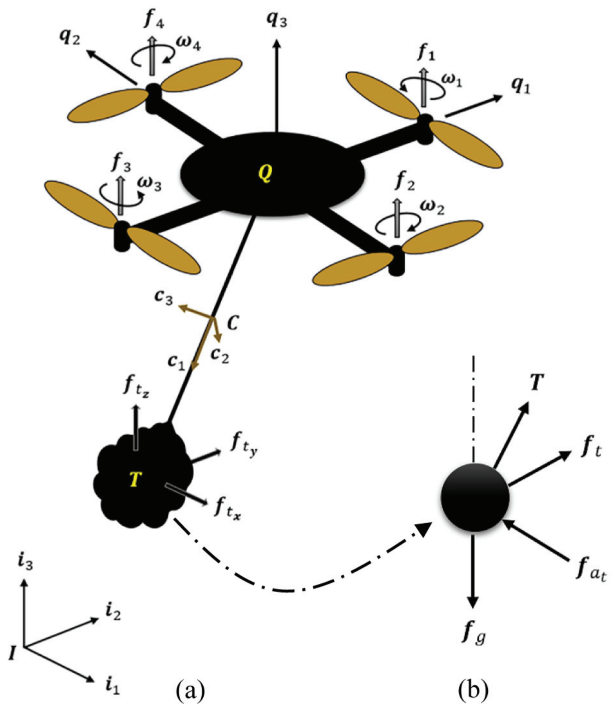

Fig. 2. (a) NTAV in the transporting phase and (b) Free body diagram (FBD) of the trapped target based on Assumption 5.

where e represents the restitution coefficient. By inserting the equivalent expression of $\boldsymbol{v}^I_{Q_{J_2}}$ and $\boldsymbol{v}^I_{T_2}$ from Eqs. (14) and (15) into relation (16), the impulse is obtained as follows:

$$\delta = \frac{m_T(m_Q + m_J)(1+e)}{m_Q + m_J + m_T}(\boldsymbol{v}^I_{T_1} - \boldsymbol{v}^I_{Q_{J_1}}) \cdot \boldsymbol{c}_1. \tag{17}$$

Placing the above relation in Eqs. (14) and (15), $\boldsymbol{v}^I_{Q_{J_2}}$ and $\boldsymbol{v}^I_{T_2}$ can be extracted.

Since the impulse passes through the connection point of the cable to the jet, H, it causes an angular impulse around the instantaneous c.g of the quadrotor-jet assembly, Q_J, as follows:

$$\boldsymbol{h}_\delta = \boldsymbol{S}_{HQ_J}\boldsymbol{\delta}, \tag{18}$$

where $\boldsymbol{\delta} = \delta\boldsymbol{c}_1$.

2.3. *Transporting phase*

Considering the complete twisting of the net around the target and based on Assumption 5, the dynamics of the flying system can be approximated as a cable-transport quadrotor according to Fig. 2(a). In this regard, the body frame of cable, $\boldsymbol{C}$, is defined with unit vectors $(\boldsymbol{c}_1, \boldsymbol{c}_2, \boldsymbol{c}_3)$ in which the first unit is tangent to the cable toward the trapped target, the second unit perpendicular to the first one and on the inertial horizontal plane and the third one complements the right-handed system. In this respect, the cable's Euler angles (β, λ) are added to the states of the system (Appendix A) [28].

Remark 1. In order to avoid strong torques on the jet servos in the capturing and transporting phases, the servos become free at the moment of engagement. In this condition, the jet Euler angles (χ, γ) are measured directly with respect to the inertial coordinate system as we have it for the cable body frame.

Assumption 7. The cable is inflexible and unstretchable during the smooth transporting phase.

In order to do a kinetic analysis, the system is divided into three subsystems: 1. Quadrotor, 2. Jet and 3. Cable-target set. The governing equations of quadrotor are expressed as

$$m_Q D^I \boldsymbol{v}^I_Q = \boldsymbol{f} + \boldsymbol{f}_e + \boldsymbol{f}_{a_q} + m_Q\boldsymbol{g}, \tag{19}$$

$$D^Q(\boldsymbol{I}^Q_Q\boldsymbol{\omega}^{QI}) + \boldsymbol{\Omega}^{QI}(\boldsymbol{I}^Q_Q\boldsymbol{\omega}^{QI}) = \boldsymbol{\tau} + \boldsymbol{S}_{EQ}\boldsymbol{f}_e + \boldsymbol{\tau}_{gyr}. \tag{20}$$

The dynamics of the jet is obtained as

$$m_J D^I \boldsymbol{v}^I_J = \boldsymbol{f}_e + \boldsymbol{T} + m_J\boldsymbol{g}, \tag{21}$$

$$\begin{aligned} &D^J(\boldsymbol{I}^J_J\boldsymbol{\omega}^{JI}) + \boldsymbol{\Omega}^{JI}(\boldsymbol{I}^J_J\boldsymbol{\omega}^{JI}) + m_J\boldsymbol{S}_{JE}D^I\boldsymbol{v}^I_J \\ &\quad = \boldsymbol{\tau}_{d_j} + \boldsymbol{S}_{HE}\boldsymbol{T} + m_J\boldsymbol{S}_{JE}\boldsymbol{g}, \end{aligned} \tag{22}$$

where $\boldsymbol{T}$ is the tensile force of the cable (The letter T also indicates the c.g of the trapped target as shown in Fig. 2(a)). Utilizing Newton–Euler laws for the suspended trapped target, one gets

$$\begin{aligned} &m_C D^I\boldsymbol{v}^I_C + m_T D^I \boldsymbol{v}^I_T \\ &\quad = \boldsymbol{T} + \boldsymbol{f}_{a_c} + \boldsymbol{f}_{a_t} + \boldsymbol{f}_t + (m_C + m_T)\boldsymbol{g}, \end{aligned} \tag{23}$$

$$\begin{aligned} &D^C(\boldsymbol{I}^C_C\boldsymbol{\omega}^{CI}) + \boldsymbol{\Omega}^{CI}(\boldsymbol{I}^C_C\boldsymbol{\omega}^{CI}) + m_C\boldsymbol{S}_{CH}D^I\boldsymbol{v}^I_C + m_T\boldsymbol{S}_{TH}D^I\boldsymbol{v}^I_T \\ &\quad = \boldsymbol{\tau}_{d_c} + \boldsymbol{S}_{CH}\boldsymbol{f}_{a_c} + \boldsymbol{S}_{TH}\boldsymbol{f}_{a_t} + \boldsymbol{S}_{TH}\boldsymbol{f}_t + m_C\boldsymbol{S}_{CH}\boldsymbol{g} + m_T\boldsymbol{S}_{TH}\boldsymbol{g}, \end{aligned} \tag{24}$$

where $\boldsymbol{f}_t$ represents the force applied by the target as illustrated in Fig. 2 and $\boldsymbol{\tau}_{d_c}$ is the dissipative moment at the connection point of the cable and jet which is obtained as

$$\boldsymbol{\tau}_{d_c} = -C_{d_c}\boldsymbol{\omega}^{CI}, \tag{25}$$

also $\boldsymbol{f}_{a_c}$ and $\boldsymbol{f}_{a_t}$ are the aerodynamic drag force acting on the cable and trapped target, respectively, which are expressed as follows [29, 30]:

$$\begin{aligned} \boldsymbol{f}_{a_c} = &-\frac{1}{2}\rho d_c l_c(\pi C_{D_t}(\boldsymbol{v}^I_C \cdot \boldsymbol{c}_1)|\boldsymbol{v}^I_C \cdot \boldsymbol{c}_1| \cdot \boldsymbol{c}_1 \\ &+ C_{D_n}(\boldsymbol{v}^I_C - (\boldsymbol{v}^I_C \cdot \boldsymbol{c}_1)\boldsymbol{c}_1)|\boldsymbol{v}^I_C - (\boldsymbol{v}^I_C \cdot \boldsymbol{c}_1)\boldsymbol{c}_1|), \end{aligned} \tag{26}$$

$$\begin{aligned} \boldsymbol{f}_{a_t} = &-\frac{1}{2}\rho A_T C_{D_T}((\boldsymbol{v}^I_T \cdot \boldsymbol{c}_1)|\boldsymbol{v}^I_T \cdot \boldsymbol{c}_1|\boldsymbol{c}_1 \\ &+ (\boldsymbol{v}^I_T - (\boldsymbol{v}^I_T \cdot \boldsymbol{c}_1)\boldsymbol{c}_1)|\boldsymbol{v}^I_T - (\boldsymbol{v}^I_T \cdot \boldsymbol{c}_1)\boldsymbol{c}_1|), \end{aligned} \tag{27}$$

where C_{d_c} indicates the dissipative coefficient at the connection point (which can be omitted due to its smallness), C_{D_t} and C_{D_n} represent tangential and normal drag coefficients of the cable, and d_c and l_c are the cable's diameter and length. In this regard, C_{D_T} is the drag coefficient of the trapped target and $A_T = \pi d_T^2/4$ is the drag reference area in which d_T represents the trapped target's diameter based on the model illustrated in Fig. 2(b).

2.4. *Fast maneuvering phase*

In some flight conditions, quadrotor performs an agile maneuver in which the tension in the cable becomes zero for a few moments and the target exerts an impact on the vehicle during re-engagement. According to the FBD of the trapped target in Fig. 2(b), the governing equation is equal to

$$m_T D^I\boldsymbol{v}^I_T = \boldsymbol{T} + \boldsymbol{f}_{a_t} + \boldsymbol{f}_t + m_T\boldsymbol{g}. \tag{28}$$

Since the tension of the cable is in line with the longitudinal axis of the cable, the value of $\boldsymbol{T}$ based on other terms in this direction is equal

$$\boldsymbol{T} \cdot \boldsymbol{c}_1 = m_T D^I\boldsymbol{v}^I_T \cdot \boldsymbol{c}_1 - \boldsymbol{f}_{a_t} \cdot \boldsymbol{c}_1 - \boldsymbol{f}_t \cdot \boldsymbol{c}_1 - m_T\boldsymbol{g} \cdot \boldsymbol{c}_1 \tag{29}$$

where $\boldsymbol{c}_1$ is obtained as follows:

$$\boldsymbol{c}_1 = \frac{\boldsymbol{s}_{TI} - \boldsymbol{s}_{HI}}{\|\boldsymbol{s}_{TI} - \boldsymbol{s}_{HI}\|}. \tag{30}$$

Table 1. The values of the aerial system parameters.

Parameter	Value	Unit
(m_Q, m_J)	$(0.5, 0.05)$	kg
(m_C, m_{Net})	$(0.003, 0.020)$	kg
(m_N, m_{T_r}, m_T)	$(0.023, 0.24, 0.26)$	kg
J_r	$3.357e^{-5}$	$\text{kg}\cdot\text{m}^2$
$(I_{q_{11}}, I_{q_{22}}, I_{q_{33}})$	$(2.32, 2.32, 4.0)e^{-3}$	$\text{kg}\cdot\text{m}^2$
$(I_{j_{11}}, I_{j_{22}}, I_{j_{33}})$	$(9.13, 9.32, 9.32)e^{-6}$	$\text{kg}\cdot\text{m}^2$
$(I_{n_{11}}, I_{n_{22}}, I_{n_{33}})$	$(5.75, 3.91, 3.91)e^{-6}$	$\text{kg}\cdot\text{m}^2$
$(I_{c_{11}}, I_{c_{22}}, I_{c_{33}})$	$(0.00003375, 3.6, 3.6)e^{-4}$	$\text{kg}\cdot\text{m}^2$
$(\lvert s_{EQ}\rvert, \lvert s_{JE}\rvert)$	$(0.01, 0.015)$	m
$(\lvert s_{HE}\rvert, \lvert s_{NE}\rvert)$	$(0.02, 0.035)$	m
$(\lvert v_N^I\rvert, \Delta t, e)$	$(5, 0.05, 0.8)$	$(\text{m/s}, \text{s}, -)$
(l_c, d_c, d_T)	$(1.2, 0.003, 0.12)$	m
(A_Q, A_N, A_T)	$(0.06125, 0.15, 0.01131)$	m^2
$(C_{D_{q_1}}, C_{D_{q_2}}, C_{D_{q_3}})$	$(0.2, 0.2, 0.3)$	–
$(C_{D_{n_1}}, C_{D_{n_2}}, C_{D_{n_3}})$	$(0.25, 0.04, 0.04)$	–
$(C_{D_t}, C_{D_n}, C_{D_T})$	$(0.01, 1, 0.6)$	–
(C_{d_j}, C_{d_c})	$(0.001, 0)$	$\text{N}\cdot\text{m}\cdot\text{s}$

Considering $\boldsymbol{T} = -T\boldsymbol{c}_1$, the cable is in a slack state ($T \leq 0$) if

$$m_T D^I \boldsymbol{v}_T^I \cdot \boldsymbol{c}_1 - \boldsymbol{f}_{a_t} \cdot \boldsymbol{c}_1 - \boldsymbol{f}_t \cdot \boldsymbol{c}_1 - m_T \boldsymbol{g} \cdot \boldsymbol{c}_1 \geq 0. \tag{31}$$

In this condition, the dynamics of the quadrotor and target are separated for a moment and the target starts projectile motion as depicted in Eq. (13). The distance between the attachment point to the aerial vehicle and the target cannot exceeds the cable's length

$$\|\boldsymbol{s}_{TI} - \boldsymbol{s}_{HI}\| \leq l_c. \tag{32}$$

This condition prevails until the distance between these two objects becomes equal to the length of the cable. At this moment, a collision occurrs and the dynamic coupling is re-established. In order to evaluate the collision, Eqs. (14)–(18) are applied. In Table 1 the assigned values of the system parameters are presented [31–33]. The values of ρ and g are considered 1.225 kg/m^3 and 9.80665 m/s^2, respectively.

The quantities $I_{k_{11}}$, $I_{k_{22}}$ and $I_{k_{33}}$, $k = q, j, n, c$ in Table 1, represent the principal moments of inertia of each body.

3. Control System

In this paper, the main objective of the control system design is precise tracking control of the flying vehicle after capturing a flying object. Hereupon, the control of the system in pursuit and capturing phases are carried out based on predetermined scenario in which upon observing the target, the aerial robot starts flying from a stationary state, approaches the target and performs the act of capturing.

Since, in a smooth transportation, the trapped target follows approximately a parallel trajectory as the c.g of the aerial vehicle moves on with a distance apart approximately equal to the length of the cable, the attitude dynamics of the cable-net-target set along with the forces applied by the oscillatory target can be regarded as external time-varying loads applied on the air vehicle in its overall translational motion. Regarding the fact that there is no predesigned information about the exact value of the target's mass which appears explicitly in translational dynamics together with the lack of knowledge about the exact distance between the quadrotor and the target due to the unknown final trapping form of the net and also aerodynamics characteristics of the trapped target, the model uncertainties can be intensified and led to a noticeable tracking error.

Regarding the nonlinear nature of NTAV dynamics that is exposed to the intense disturbances and uncertainties and considering high robustness, consistency and fast transient response of SMC [34–36], an advanced version of this control approach i.e. GSTSMC is designed for this under-actuated flying robot to enable the system to track nominal trajectories in the presence of such a strong load. In this regard, an accurate estimation of target's mass is provided via applying an estimator in control algorithm, which leads to precise tracking of the nominal trajectories. For the sake of simplicity, without loss of generality, it is tried to decouple the vehicle's translational dynamics from other states by considering $|\boldsymbol{s}_{EQ}| = 0$ in our control model, which means the jet connection point is compatible with the c.g of the quadrotor. Although this issue leads to complete decoupling in transporting phase, it leads to an incomplete decoupling in other phases due to the dependence of the jet dynamics on the vehicle's attitude one. Since these coupling terms are small, it is tried to obtain an appropriate structure of the translational dynamics in these phases by eliminating these terms. The general control scheme is illustrated in Fig. 3.

Remark 2. The assumption $|\boldsymbol{s}_{EQ}| = 0$ in the control model, leads to the elimination of some dynamic terms compared to the extracted model that although they are relatively small in the pursuit phase, it significantly intensifies the effect of the suspended trapped target and impulsive forces caused by the throwing net and different velocities of the vehicle and flying object, which the control system must be robust to, and preserves the stability and precise tracking in this condition.

Considering $\boldsymbol{X}_1 = [x\ y\ z]^T$ and $\boldsymbol{u} = [v_x\ v_y\ v_z]^T$ as control inputs in which v_x, v_y and v_z are virtual control signals, which are defined as

$$v_x = (C_\psi S_\theta C_\phi + S_\psi S_\phi)u_1, \tag{33}$$

$$v_y = (S_\psi S_\theta C_\phi - C_\psi S_\phi)u_1, \tag{34}$$

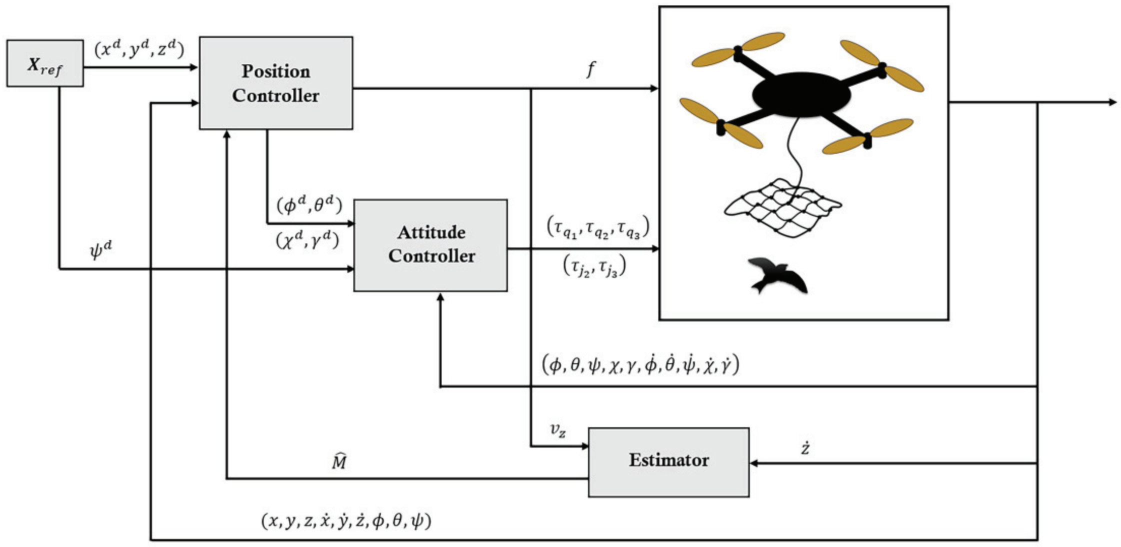

Fig. 3. Schematic of the control system for the NTAV.

$$v_z = C_\theta C_\phi u_1 - Mg, \tag{35}$$

where, S_k and C_k, $k = \phi, \theta, \psi$ represent $\sin(k)$ and $\cos(k)$ and $u_1 = f = \sqrt{v_x^2 + v_y^2 + (v_z + Mg)^2}$ indicates the total thrust force generated by rotors, and the direct impact form of the system's translational dynamics can be written as follows:

$$\begin{cases} \dot{\boldsymbol{X}}_1 = \boldsymbol{X}_2, \\ \dot{\boldsymbol{X}}_2 = \widehat{\boldsymbol{F}}(\boldsymbol{X}) + \widehat{\boldsymbol{G}}(\boldsymbol{X})\boldsymbol{u} + \widehat{\boldsymbol{L}}(\boldsymbol{X}, t), \end{cases} \tag{36}$$

where $\boldsymbol{X} = [\boldsymbol{X}_1 \ \boldsymbol{X}_2]^T$ is the state vector and $\widehat{\boldsymbol{F}}(\boldsymbol{X}) + \widehat{\boldsymbol{G}}(\boldsymbol{X})\boldsymbol{u}$ represents the known affine model of the flying system. In this regard, $\widehat{\boldsymbol{L}}$ is the vector of lumped time-varying disturbances and uncertainties. The terms $\widehat{\boldsymbol{F}}(\boldsymbol{X})$ and $\widehat{\boldsymbol{G}}(\boldsymbol{X})$ are obtained as

$$\widehat{\boldsymbol{F}}(\boldsymbol{X}) = \begin{bmatrix} M & 0 & 0 \\ 0 & M & 0 \\ 0 & 0 & M \end{bmatrix}^{-1} \begin{bmatrix} f_{a_{q_x}} \\ f_{a_{q_y}} \\ f_{a_{q_z}} \end{bmatrix}, \tag{37}$$

$$\widehat{\boldsymbol{G}}(\boldsymbol{X}) = \begin{bmatrix} M & 0 & 0 \\ 0 & M & 0 \\ 0 & 0 & M \end{bmatrix}^{-1}, \tag{38}$$

where M represents the effective mass in each phase which is equal to $m_Q + m_J + m_N$ in pursuit phase, $m_Q + m_J$ in the capturing phase and $m_Q + m_J + m_N + m_{T_r}$ in the transporting phase.

Based on relations (33) to (35), the reference trajectories of roll and pitch dynamics can be calculated as follows:

$$\phi^d = \arcsin\left(\frac{v_x S_\psi - v_y C_\psi}{u_1}\right), \tag{39}$$

$$\theta^d = \arctan\left(\frac{v_x C_\psi + v_y S_\psi}{v_z + Mg}\right). \tag{40}$$

Considering $\boldsymbol{X}_1 = [\phi \ \theta \ \psi]^T$ and $\boldsymbol{u} = [\tau_{q_1} \ \tau_{q_2} \ \tau_{q_3}]^T$ in which τ_{q_1}, τ_{q_2} and τ_{q_3} indicate roll, pitch and yaw moments, respectively, the elements of Eq. (36) for attitude dynamics of quadrotor in transporting phase are equal to

$$\widehat{\boldsymbol{F}}(\boldsymbol{X}) = \begin{bmatrix} I_\phi & 0 & I_k \\ 0 & I_\theta & I_l \\ I_k & I_l & I_\psi \end{bmatrix}^{-1} \begin{bmatrix} h_\phi + \tau_{\mathrm{gyr}_1} \\ h_\theta + \tau_{\mathrm{gyr}_2} C_\phi \\ h_\psi - \tau_{\mathrm{gyr}_1} S_\theta + \tau_{\mathrm{gyr}_2} S_\phi C_\theta \end{bmatrix}, \tag{41}$$

$$\widehat{\boldsymbol{G}}(\boldsymbol{X}) = \begin{bmatrix} I_\phi & 0 & I_k \\ 0 & I_\theta & I_l \\ I_k & I_l & I_\psi \end{bmatrix}^{-1} \begin{bmatrix} 1 & 0 & 0 \\ 0 & C_\phi & -S_\phi \\ -S_\theta & S_\phi C_\theta & C_\phi C_\theta \end{bmatrix}. \tag{42}$$

In Table 2 the equivalent terms in above relations are expressed.

Assumption 8. The uncertainties are in the range space of the control matrix $\widehat{\boldsymbol{G}}(\boldsymbol{X})$ [37].

Remark 3. The servos of the jet are active in the pursuit phase and there is a complete dynamic coupling between attitude motions of the jet and the quadrotor. Therefore, the adjustment of the jet aiming direction is performed based on the quadrotor attitude angles and the position of the aerial vehicle relative to the flying target. For instance, if the system is flying in forward motion with attitude angles $\phi(t) = 0$ and $\psi(t) = 0$ and the aiming direction is wanted to be vertically downward, this goal is realized by defining the reference inputs as $\lambda^d(t) = 0$ and $\chi^d(t) = \theta(t)$ for these channels.

Table 2. The equivalent terms in Eqs. (41) and (42).

Parameter	Equivalent term
h_a	$I_{q_{22}} - I_{q_{33}}$
h_b	$I_{q_{11}} + (I_{q_{22}} - I_{q_{33}})C_{2\phi}$
h_c	$I_{q_{11}} - (I_{q_{22}} - I_{q_{33}})C_{2\phi}$
h_d	$I_{q_{11}} - I_{q_{22}}S_\phi^2 - I_{q_{33}}C_\phi^2$
h_ϕ	$h_b C_\theta \dot\theta\dot\psi - h_a S_\phi C_\phi \dot\theta^2 + h_a C_\theta^2 S_\phi C_\phi \dot\psi^2$
h_θ	$h_a S_{2\phi}\dot\phi\dot\theta - h_b C_\theta \dot\phi\dot\psi + h_d S_\theta C_\theta \dot\psi^2$
h_ψ	$h_c C_\theta \dot\phi\dot\theta - h_d S_{2\theta}\dot\theta\dot\psi + h_a(S_\theta \dot\theta^2/2 - C_\theta^2\dot\phi\dot\psi)S_{2\phi}$
I_k	$-I_{q_{11}}S_\theta$
I_l	$(I_{q_{22}} - I_{q_{33}})C_\theta S_\phi C_\phi$
I_ϕ	$I_{q_{11}}$
I_θ	$I_{q_{22}}C_\phi^2 + I_{q_{33}}S_\phi^2$
I_ψ	$I_{q_{11}}S_\theta^2 + (I_{q_{22}}S_\phi^2 + I_{q_{33}}C_\phi^2)C_\theta^2$
τ_{gyr_1}	$J_r(\dot\theta C_\phi + \dot\psi S_\phi C_\theta)\sum_\omega$
τ_{gyr_2}	$-J_r(\dot\phi - \dot\psi S_\theta)\sum_\omega$

3.1. *Generalized super-twisting sliding mode control*

The GSTSMC, as a developed version of super-twisting control law, contains extra correction terms in its algorithm, which significantly improves the performance of the controller in terms of robustness, convergence rate and steady-state error [38–40]. Considering the matching condition is established as declared in Assumption 8, the algorithm in Moreno [38] can be extended for the MIMO nonlinear flying system. In this respect, the sliding surface for position dynamics is defined as follows:

$$\boldsymbol{\sigma} = \dot{\boldsymbol{e}}(t) + \boldsymbol{\lambda}\boldsymbol{e}(t) \tag{43}$$

where $\boldsymbol{e} = \boldsymbol{X}_1 - \boldsymbol{X}_1^d$ and $\dot{\boldsymbol{e}} = \boldsymbol{X}_2 - \boldsymbol{X}_2^d = \dot{\boldsymbol{X}}_1 - \dot{\boldsymbol{X}}_1^d$ indicate error vector and its rate. Getting time derivative of sliding surface and applying GSTSMC law as

$$\boldsymbol{u} = \widehat{\boldsymbol{G}}(\boldsymbol{X})^{-1}\left(\ddot{\boldsymbol{X}}_1^d - \widehat{\boldsymbol{F}}(\boldsymbol{X}) - \boldsymbol{\lambda}\dot{\boldsymbol{e}} - \boldsymbol{K}_1\boldsymbol{\Lambda}_1 - \boldsymbol{K}_2\int_0^t \boldsymbol{\Lambda}_2 d\tau\right) \tag{44}$$

in which

$$\begin{cases} \boldsymbol{\Lambda}_1(\boldsymbol{\sigma}) = \boldsymbol{\eta}_1|\boldsymbol{\sigma}|^{\frac{1}{2}}\text{sign}(\boldsymbol{\sigma}) + \boldsymbol{\eta}_2\boldsymbol{\sigma}, \\ \boldsymbol{\Lambda}_2(\boldsymbol{\sigma}) = \dfrac{1}{2}\boldsymbol{\eta}_1^2\text{sign}(\boldsymbol{\sigma}) + \dfrac{3}{2}\boldsymbol{\eta}_1\boldsymbol{\eta}_2|\boldsymbol{\sigma}|^{\frac{1}{2}}\text{sign}(\boldsymbol{\sigma}) + \boldsymbol{\eta}_2^2\boldsymbol{\sigma}, \end{cases} \tag{45}$$

one obtains

$$\begin{cases} \dot{\boldsymbol{\sigma}} = -\boldsymbol{K}_1\boldsymbol{\Lambda}_1(\boldsymbol{\sigma}) + \boldsymbol{\Gamma}, \\ \dot{\boldsymbol{\Gamma}} = -\boldsymbol{K}_2\boldsymbol{\Lambda}_2(\boldsymbol{\sigma}) + \varrho, \\ \varrho = \dot{\widehat{\boldsymbol{L}}}. \end{cases} \tag{46}$$

The coefficients in Eqs. (43)–(46) are as $\boldsymbol{J} = \text{diag}([j_x\ j_y\ j_z])$ with positive constant elements in which $j = \lambda, k_1, k_2, \eta_1, \eta_2$. As seen, GSTSMC like GSMC ($\boldsymbol{u} = \widehat{\boldsymbol{G}}(\boldsymbol{X})^{-1}(\ddot{\boldsymbol{X}}_1^d - \widehat{\boldsymbol{F}}(\boldsymbol{X}) - \boldsymbol{\lambda}\dot{\boldsymbol{e}} - \boldsymbol{\varepsilon}\text{sign}(\boldsymbol{\sigma}) - \boldsymbol{K}\boldsymbol{\sigma})$ where $\boldsymbol{\varepsilon} = \text{diag}([\varepsilon_x\ \varepsilon_y\ \varepsilon_z])$ and $\boldsymbol{K} = \text{diag}([k_x\ k_y\ k_z])$) has linear stabilizing terms, including $\boldsymbol{\eta}_2$ in its algorithm. If $\boldsymbol{\eta}_1 = \boldsymbol{I}$ and $\boldsymbol{\eta}_2 = \boldsymbol{0}$ are considered, the standard STSMC is extracted.

In order to prove $(\boldsymbol{\sigma}, \boldsymbol{\Gamma}) \to (\boldsymbol{0}, \boldsymbol{0})$ in finite time, the Lyapunov candidate is selected in the following form:

$$\begin{cases} V = \boldsymbol{\zeta}^T\boldsymbol{P}\boldsymbol{\zeta} \\ \boldsymbol{\zeta}^T = [\boldsymbol{\zeta}_x^T \quad \boldsymbol{\zeta}_y^T \quad \boldsymbol{\zeta}_z^T] \\ \boldsymbol{P} = \text{diag}([\boldsymbol{P}_x \quad \boldsymbol{P}_y \quad \boldsymbol{P}_z]) \end{cases} \tag{47}$$

where $\boldsymbol{\zeta}_i^T = [\Lambda_{1_i}(\sigma_i)\ \Gamma_i]$ and $\boldsymbol{P}_i$ is a $2*2$ positive definite matrix. According to the quadratic form of the Lyapunov function (47), we have

$$\lambda_{min}(\boldsymbol{P}_i)\|\boldsymbol{\zeta}_i\|_2^2 \le V_i \le \lambda_{max}(\boldsymbol{P}_i)\|\boldsymbol{\zeta}_i\|_2^2 \quad i = x, y, z. \tag{48}$$

In the above relation, $\|\boldsymbol{\zeta}_i\|_2^2$ is the Euclidean norm of $\boldsymbol{\zeta}_i$. Considering that $\Lambda_{2_i}(\sigma_i) = \Lambda'_{1_i}(\sigma_i)\Lambda_{1_i}(\sigma_i)$, one gets

$$\dot{\boldsymbol{\zeta}}_i = \Lambda'_{1_i}(\sigma_i)(\boldsymbol{A}_i\boldsymbol{\zeta}_i + \boldsymbol{B}_i\tilde{\varrho}_i) \tag{49}$$

where $\tilde{\varrho}_i = 2|\sigma_i|^{\frac{1}{2}}\varrho_i/(\eta_{1_i} + 2\eta_{2_i}|\sigma_i|^{\frac{1}{2}})$, $B_i^T = [0\ 1]$ and $A_i = [-k_{1_i}\ 1;\ -k_{2_i}\ 0]$.

Assumption 9. ϱ_i is uniformly bounded so that $2|\varrho_i| \le \delta_i$.

Based on Assumption 9, it can be shown that $|\tilde{\varrho}_i| \le \delta_i|\zeta_{i_1}|$ when $\eta_{1_i} = 1$, which means $\upsilon_i(\boldsymbol{\zeta}_i, \tilde{\varrho}_i) = \delta_i^2\zeta_{i_1}^2 - \tilde{\varrho}_i^2 \ge 0$. This relation can be written as follows:

$$\upsilon_i(\boldsymbol{\zeta}_i, \tilde{\varrho}_i) = \begin{bmatrix} \boldsymbol{\zeta}_i \\ \tilde{\varrho}_i \end{bmatrix}^T \begin{bmatrix} \boldsymbol{R}_i & \boldsymbol{\chi}_i^T \\ \boldsymbol{\chi}_i & -\Theta_i \end{bmatrix} \begin{bmatrix} \boldsymbol{\zeta}_i \\ \tilde{\varrho}_i \end{bmatrix} \ge 0 \tag{50}$$

where $\boldsymbol{R} = \delta_i^2\boldsymbol{C}_i^T\boldsymbol{C}_i$, $\boldsymbol{C}_i = [1\ 0]$, $\boldsymbol{\chi}_i = [0\ 0]$ and $\Theta_i = 1$.

Through applying the classical circle criterion, it is proved that if the Nyquist diagram of the transfer function, $\boldsymbol{G}_i(s) = \boldsymbol{C}_i(s\boldsymbol{I} - \boldsymbol{A}_i)^{-1}\boldsymbol{B}_i$, satisfies the following constraint

$$\max|\boldsymbol{G}_i(j\omega)| < 1/\delta_i \tag{51}$$

then there exists a symmetric positive definite matrix $\boldsymbol{P}_i$ and $\epsilon_i > 0$ so that the following linear matrix inequality

$$\begin{bmatrix} \boldsymbol{A}_i^T\boldsymbol{P}_i + \boldsymbol{P}_i\boldsymbol{A}_i + \epsilon_i\boldsymbol{P}_i + \boldsymbol{R}_i & \boldsymbol{P}_i\boldsymbol{B}_i + \boldsymbol{\chi}_i^T \\ \boldsymbol{B}_i^T\boldsymbol{P}_i + \boldsymbol{\chi}_i & -\Theta_i \end{bmatrix} \le 0 \tag{52}$$

is established. It is shown that the relation (51) is fulfilled if $k_{2_i} > \delta_i$ and $k_{1_i}^2 > 2k_{2_i}$ [38].

With the time derivative of the Lyapunov function, one obtains

$$\begin{aligned}\dot{V} &= \sum \Lambda'_{1_i}(\boldsymbol{\zeta}_i^T(\boldsymbol{A}_i^T\boldsymbol{P}_i + \boldsymbol{P}_i\boldsymbol{A}_i)\boldsymbol{\zeta}_i + \tilde{\varrho}_i\boldsymbol{B}_i^T\boldsymbol{P}_i\boldsymbol{\zeta}_i + \boldsymbol{\zeta}_i^T\boldsymbol{P}_i\boldsymbol{B}_i\tilde{\varrho}_i) \\ &\leq \sum \Lambda'_{1_i}\left\{\begin{bmatrix}\boldsymbol{\zeta}_i \\ \tilde{\varrho}_i\end{bmatrix}^T \begin{bmatrix}\boldsymbol{A}_i^T\boldsymbol{P}_i + \boldsymbol{P}_i\boldsymbol{A}_i & \boldsymbol{P}_i\boldsymbol{B}_i \\ \boldsymbol{B}_i^T\boldsymbol{P}_i & 0\end{bmatrix}\begin{bmatrix}\boldsymbol{\zeta}_i \\ \tilde{\varrho}_i\end{bmatrix} + \upsilon_i(\boldsymbol{\zeta}_i, \tilde{\varrho}_i)\right\} \\ &\leq \sum \Lambda'_{1_i}\left\{\begin{bmatrix}\boldsymbol{\zeta}_i \\ \tilde{\varrho}_i\end{bmatrix}^T \begin{bmatrix}\boldsymbol{A}_i^T\boldsymbol{P}_i + \boldsymbol{P}_i\boldsymbol{A}_i + \boldsymbol{R}_i & \boldsymbol{P}_i\boldsymbol{B}_i + \boldsymbol{\chi}_i^T \\ \boldsymbol{B}_i^T\boldsymbol{P}_i + \boldsymbol{\chi}_i & -\Theta_i\end{bmatrix}\begin{bmatrix}\boldsymbol{\zeta}_i \\ \tilde{\varrho}_i\end{bmatrix}\right\} \\ &\leq \sum -\Lambda'_{1_i}\epsilon_i\boldsymbol{\zeta}_i^T\boldsymbol{P}_i\boldsymbol{\zeta}_i = -\sum \Lambda'_{1_i}\epsilon_i V_i \leq -\alpha V^{\frac{1}{2}} - \beta V,\end{aligned} \tag{53}$$

where $\alpha = min(\eta_{1_i}\epsilon_i\lambda_{min}^{\frac{1}{2}}(\boldsymbol{P}_i)/2)$ and $\beta = \min(\eta_{2_i}\epsilon_i)$. Hence, finite time convergence to the origin is guaranteed.

Obtaining ϕ^d and θ^d from Eqs. (39) and (40) and determining ψ^d as the reference signals of the vehicle attitude dynamics, via applying the control law similar to (44) based on attitude control signals i.e $\boldsymbol{u} = [\tau_{q_1}\ \tau_{q_2}\ \tau_{q_3}]^T$, the finite time convergence of attitude dynamics is proved. With a similar process, the attitude control law for the pursuit phase based on the presented control model in Appendix B is obtained.

One of the advantages of STSMC compared to conventional SMC is attenuating chattering of control signals. However, these destructive phenomena cannot be eradicated completely via applying this approach [41]. In order to rectify this problem, the sign function is replaced with the saturation function as follows:

$$\text{sat}(\sigma_i) = \begin{cases}\text{sign}(\sigma_i) & |\sigma_i| > \mu_i \\ \sigma_i/\mu_i & \text{else}\end{cases} \tag{54}$$

where μ_i is the thickness of the boundary layer [42].

3.2. *Parameter estimation*

Based on the expressed control strategy, if the whole dynamics of the suspended target is considered as an uncertain time-varying load, high gain values should be assigned to the controller to prevent instability and reduce tracking error, which noticeably increases control effort. Since the target mass appears in the translational equations, the degree of uncertainties and disturbances has significantly reduced only by considering the attitude dynamics of the set as a time-varying load. Regarding the fact that stimulating the height channel is easier than longitudinal and lateral ones, this dynamics is used for parameter estimation. In this regard, defining $w = \dot{z}$ and considering $C_z\dot{z}$ as an auxiliary term to help estimator formulation in which C_z is a dissipative coefficient, the governing equation of altitude channel can be written as follows:

$$\dot{w} + aw = bu_z \tag{55}$$

where $u_z = v_z$, $a = C_z/M$ and $b = 1/M$. In this study, due to the high efficiency of least squares (LS) method, this algorithm is used to estimate the parameter as expressed in the following equation [43].

$$\begin{cases}\dot{\boldsymbol{\vartheta}} = \mathcal{P}\boldsymbol{\varphi}\boldsymbol{e}, \\ \dot{\mathcal{P}} = \kappa\mathcal{P} - \mathcal{P}\boldsymbol{\varphi}\boldsymbol{\varphi}^T\mathcal{P},\end{cases} \tag{56}$$

where $\boldsymbol{\vartheta}$, $\boldsymbol{\varphi}$ and $\boldsymbol{e}$ are the vectors of estimated parameters, input-output signals and prediction errors and $\mathcal{P}$ and κ are the covariance matrix and forgetting factor, respectively. In order to avoid numerical problem, the vectors $\boldsymbol{\varphi}$ and $\boldsymbol{\vartheta}_0$ are obtained via filtering signals as relation (57) in which ι is a positive constant.

$$\begin{cases}\boldsymbol{\varphi}^T = [v \quad q], \\ \boldsymbol{\vartheta}_0 = [\iota - a \quad b], \\ v = \dfrac{1}{s+\iota}w; \quad q = \dfrac{1}{s+\iota}u_z.\end{cases} \tag{57}$$

4. Performance Evaluation

In this section, the performance of the designed controller is investigated through the simulation in MATLAB. In this regard, it is assumed that the system is initially at rest in the origin of inertial coordinate system and starts to fly when the flying target is in the position $(x_t(0), y_t(0), z_t(0)) = (20, 2, 3.5)$ with the constant velocity $(\dot{x}_t, \dot{y}_t, \dot{z}_t) = (3, 0, 0)$. For capturing the target, the aerial vehicle tries to reach to $y^d(t) = 2$ m and $z^d(t) = 4$ m with the speed of $\dot{x}^d(t) = 6$ m/s and throws the net downward (with $\gamma = 0$ rad and $\chi = -0.05$ rad) so that at the moment of throwing, it is approximately above the target.

As mentioned earlier, since the exact values of equivalent cable's length and target's diameter and their drag coefficients are unknown, these parameters are approximated as $(\hat{l}_c, \hat{d}_T, \hat{C}_{D_T}) = (1.1, 0.1, 0.5)$ based on the net's size and spherical model of trapped target illustrated in Figs. 1 and 2, which shows 10–20% uncertainty on these parameters compared with their nominal values shown in Table 1.

The optimal gain values of the controllers which were designed via trial and error method are presented in Table 3. In all three controllers the thicknesses of boundary layers are considered as $\mu_i = 0.2$ and $\mu_i = 0.1$ for translational and attitude states, respectively. The parameters of the estimator are set as $(a(0), b(0), \kappa, \iota) = (0, 2, 0.99, 1)$ and $\mathcal{P}(\boldsymbol{0}) = \text{diag}([10{,}000\ 10{,}000])$.

In this study, the pattern of forces applied by the target is considered as the semi-stochastic oscillations with decreasing amplitude, Fig. 4.

In the first step, the performance of the robust controllers is evaluated without considering the target's mass

Table 3. The assigned values of the controllers' gains.

GSMC		STSMC		GSTSMC			
$(\lambda_x, \lambda_y, \lambda_z)$	(1.2,1.2,2)	$(\lambda_x, \lambda_y, \lambda_z)$	(1.2,1.2,2)	$((\lambda_x, \lambda_y, \lambda_z))$	(1.2,1.2,2)	$(\eta_{1_x}, \eta_{1_y}, \eta_{1_z})$	(1,1,1)
$(\lambda_\phi, \lambda_\theta, \lambda_\psi)$	(12,12,6)	$(\lambda_\phi, \lambda_\theta, \lambda_\psi)$	(12,12,6)	$(\lambda_\phi, \lambda_\theta, \lambda_\psi)$	(12,12,6)	$(\eta_{1_\phi}, \eta_{1_\theta}, \eta_{1_\psi})$	(1,1,1)
(λ_c, λ_g)	(20,20)	(λ_c, λ_g)	(40,20)	(λ_c, λ_g)	(20,10)	(η_{1_c}, η_{1_g})	(1,1)
$(\varepsilon_x, \varepsilon_y, \varepsilon_z)$	(1,1,2)	$(k_{1_x}, k_{1_y}, k_{1_z})$	(2,2,2)	$(k_{1_x}, k_{1_y}, k_{1_z})$	(2,2,2)	$(\eta_{2_x}, \eta_{2_y}, \eta_{2_z})$	(1,1,1)
$(\varepsilon_\phi, \varepsilon_\theta, \varepsilon_\psi)$	(1,1,1)	$(k_{1_\phi}, k_{1_\theta}, k_{1_\psi})$	(2,2,2)	$(k_{1_\phi}, k_{1_\theta}, k_{1_\psi})$	(2,2,2)	$(\eta_{2_\phi}, \eta_{2_\theta}, \eta_{2_\psi})$	(1,1,8)
$(\varepsilon_c, \varepsilon_g)$	(10,10)	(k_{1_c}, k_{1_g})	(20,20)	(k_{1_c}, k_{1_g})	(10,10)	(η_{2_c}, η_{2_g})	(5,5)
(k_x, k_y, k_z)	(1,1,2)	$(k_{2_x}, k_{2_y}, k_{2_z})$	(1,1,1)	$(k_{2_x}, k_{2_y}, k_{2_z})$	(1,1,1)		
$(k_\phi, k_\theta, k_\psi)$	(2,2,2)	$(k_{2_\phi}, k_{2_\theta}, k_{2_\psi})$	(1,1,1)	$(k_{2_\phi}, k_{2_\theta}, k_{2_\psi})$	(1,1,1)		
(k_c, k_g)	(10,10)	(k_{2_c}, k_{2_g})	(1,1)	(k_{2_c}, k_{2_g})	(1,1)		

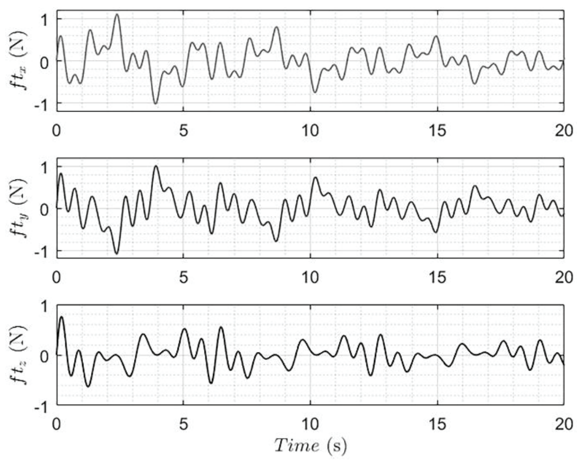

Fig. 4. Pattern of the forces generated by the target.

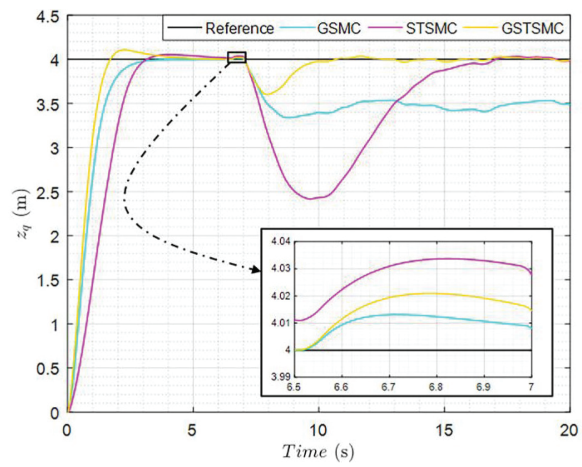

Fig. 5. The vertical motion of the quadrotor.

in their algorithm. Figures 5–7 show the simulation results for this case.

As seen in Fig. 5, the tracking quality is noticeably affected after capturing the flying object if the target's mass is not considered in control algorithm. In this regard, a significant steady-state error of 0.49 m is observed via applying GSMC and a very high altitude reduction of 1.58 m is observed through using STSMC. Although GSTSMC has considerably better tracking performance and reduced the bound of steady-state error to 0.03 m in vertical motion, the height of the flying system has decreased to 3.6 m at the moment of capturing, even by applying this algorithm. Also, oscillatory motion around the nominal path in the transporting phase is observed, which can be attributed to the high degree of uncertainty in this condition.

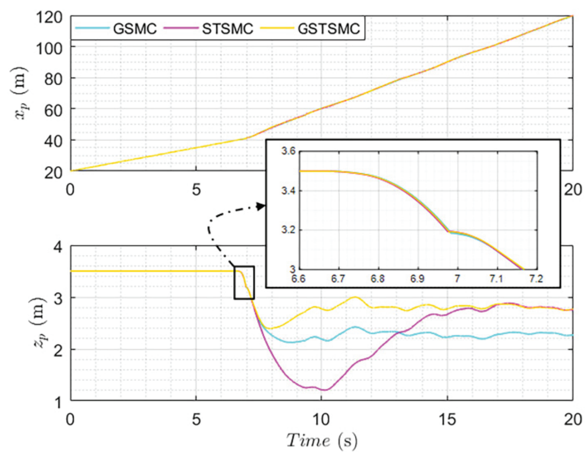

Fig. 6. The horizontal and vertical motions of the target.

As demonstrated in Figs. 5 and 7, at the moment of net shot in which a kick is applied on the multicopter, it is expected that the aerial vehicle is a bit moved upward and the thrust force is decreased at the corresponding moment by control algorithm to keep the vehicle on the path. On the other hand, considering that the target's speed is half of the flying vehicle and the multicopter maintains its horizontal speed during the mission, the slope of the target's horizontal motion is doubled after being trapped, Fig. 6.

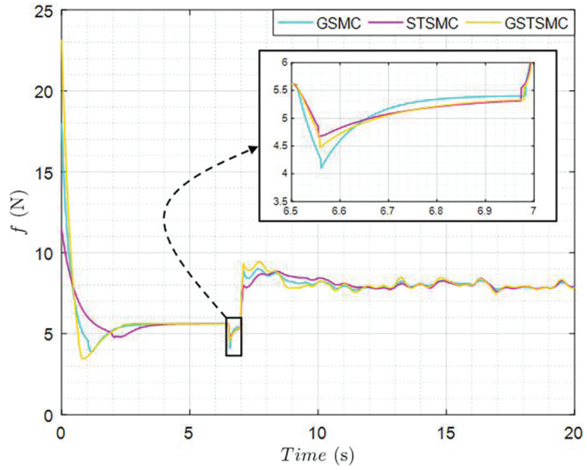

Fig. 7. Control input $u_1 = f$.

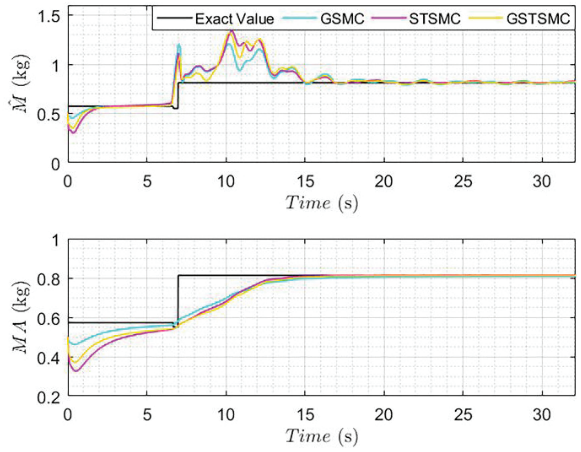

Fig. 8. Estimated parameter.

As discussed earlier, after the net hits the target, the target-net set travels freely for a while until the cable is fully opened at which the generated impulsive force changes the momentum noticeably. The tendency of the cable to place back to the vertical position has caused the height to be decreased again. Also, after capturing the target, the fluctuation of the cable is observed for a period of time after which is decreased by reducing the amplitude of forces applied by the target and the compatibility of the suspended trapped target set with the dynamics of the quadrotor in a smooth flight. These issues show the validity of the extracted model and efficiency of the designed control system.

Now, the estimator is applied to enhance the performance of the control system. Considering the fact that the estimator starts working from the beginning of the mission, its performance in pursuit and capturing phases is evaluated as well. In this respect, the stimulating input for the dynamics given in (55) is considered as relation (58) for $8\pi\,s$ after capturing the flying target. Afterward, the aerial robot continues its motion with the specified altitude and velocity.

$$z_r(t) = 4 - \cos(3t). \tag{58}$$

Considering that the model of the estimator is affected by the intensive time-varying load, $\widehat{L}_z$, in the transporting phase, the estimated parameters fluctuate around the nominal value. In order to solve this problem, the moving average (MA) of these fluctuations is calculated at each moment and given as the input to the control algorithm, which subsequently reduces the fluctuations of the estimator output as depicted in Fig. 8. At the end of the stimulating input, the average of the last 5 s of the estimated parameter is placed as the estimated value in the control algorithm and then it continues to work by interrupting the estimation loop.

The results reveal that the estimated value by GSTSMC, $\widehat{M} = 0.8120$, has less than 0.15% difference from the nominal one $M = 0.8130$. In the case of using GSMC and STSMC, this value is calculated as 0.8120 and 0.8143, respectively. Also, in the pursuit phase in which the aerial robot is affected by step input, this estimated value is obtained as 0.5828, 0.5847 and 0.5712 for GSMC, STSMC and GSTSMC, respectively. Considering the real value $M = 0.573$ in the pursuit phase, a better performance of generalized versions in estimating the parameter is observed when the system is not affected by an exciting input.

It should be noted that due to an abrupt change in the dynamics, the net shooting and target engagement process can significantly affect the accuracy of the estimator in the capturing phase, leading to undesirable divergence in estimated value. Therefore, back to the fact that most probably a vehicle will not be designed to capture targets greater than its own weight, an upper bound of the same value is considered for this time interval in the form of saturation for the estimated value feedbacked to the controller. This action has significantly attenuated the mentioned destructive effect, Fig. 8. The performance of the controllers via applying estimator are illustrated in Figs. 9–17.

According to Figs. 9–11, the efficiency of the nonlinear controllers after capturing the target has noticeably improved by estimating the target's mass. In this regard, the bounds of error in horizontal and vertical motions are obtained as $(0.049, 0.003)$, $(0.028, 0.013)$ and $(0.019, 0.008)\,m$ via GSMC, STSMC and GSTSMC, respectively, which shows an impressive enhancement in the tracking performance of the GSMC. It is also seen, the convergence rate of GSTSMC is better than two other controllers. However, a little overshoot is observed in the graphs related to the second order algorithms. Since the lateral dynamics of the whole system is affected by the suspended oscillatory

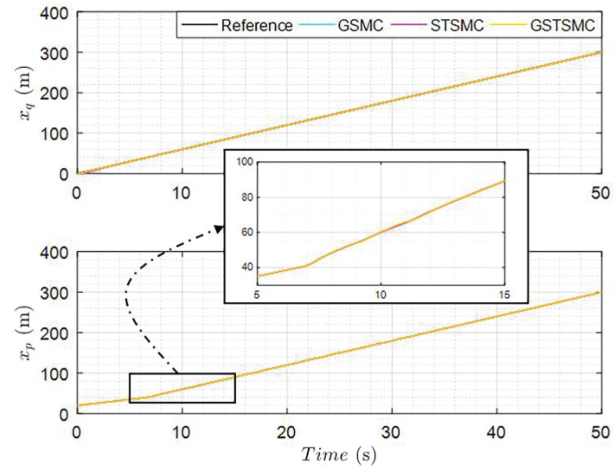

Fig. 9. Time response of x_q and x_p.

target, oscillatory motion with decreasing amplitude around predefined path is seen, Fig. 10. It is observed that the generalized versions have better performance in attenuating the oscillations and have bounded the steady state error to 0.02 m.

Based on Figs. 12–14, although the attitude dynamics of the vehicle is strongly stimulated, the variations of these angles are in an acceptable range and with the reduction of forces applied by the target and also the end of stimulating reference input, the range of fluctuations of all Euler angles decrease. In this regard, by using GSMC and especially GSTSMC, the quadrotor's attitude angles have been less affected in comparison with STSMC and the bounds of tracking error for ψ have reduced to $1.5e^{-4}$ and $5e^{-5}$ rad, respectively, which is really desirable. In this respect, via applying STSMC, the range of these variations is higher than the generalized algorithms and the tracking error has been

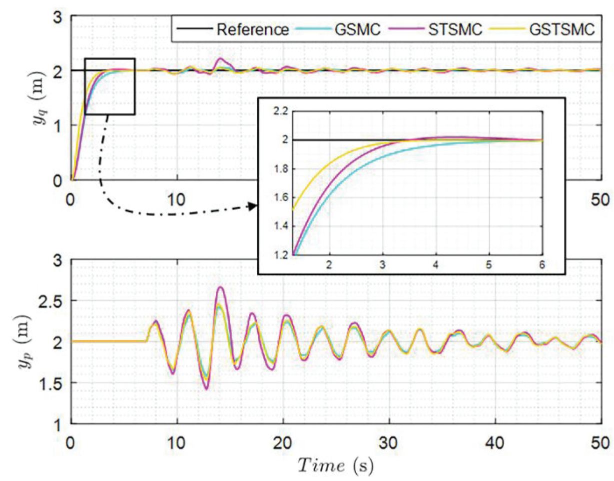

Fig. 10. Time response of y_q and y_p.

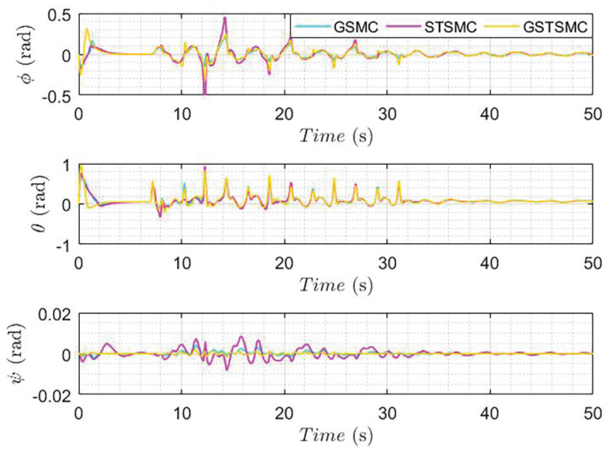

Fig. 12. Time response of ϕ, θ and ψ.

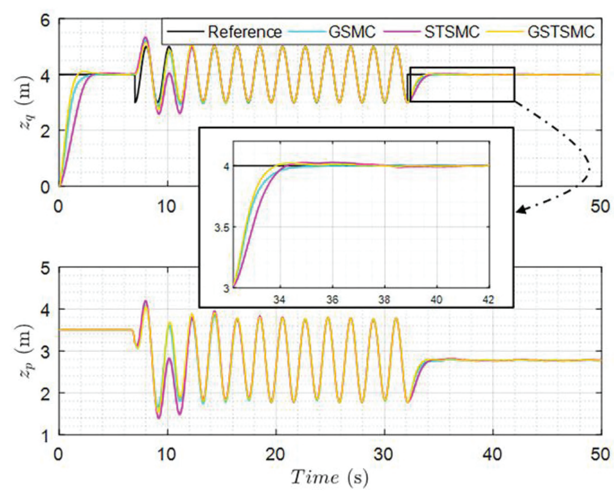

Fig. 11. Time response of z_q and z_p.

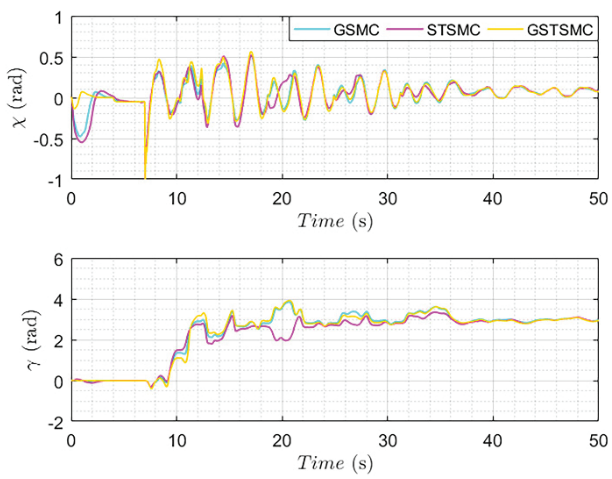

Fig. 13. Time response of χ and γ.

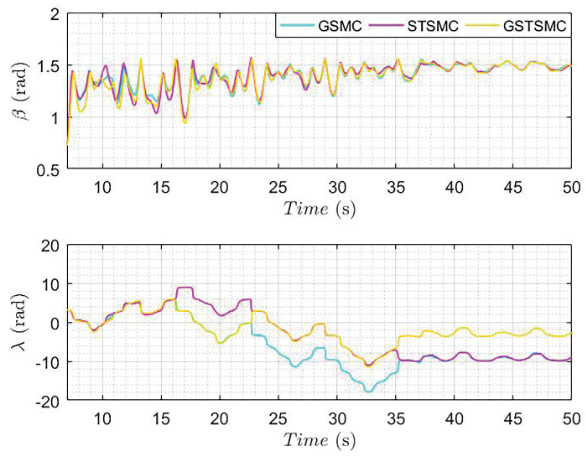

Fig. 14. Time response of β and λ.

limited to $7.5e^{-4}$ rad. This issue indicates the effective role of linear stabilizing terms in generalized robust controllers in attenuating system attitude dynamics while tracking nominal trajectories.

As seen in Fig. 14, at the initial moment of the complete opening of the cable, its attitude angles are $\lambda \approx \pi$ rad and $\beta = 0.728$ rad, respectively. It means that from the side view, the cable's angle with respect to the first direction of inertia coordinate system is $\beta' = \pi - \beta = 2.414$ rad $= 138.3°$. A complete consistency with the physics of the problem is seen regarding the facts that the quadrotor speed is twice the target speed and the capturing phase has been carried out in a short time interval. It is obvious that the β angle tends to reach $90°$ and settle down over there after the forces applied by the target are reduced. Also, the diagram related to angle λ shows that while following the stimulating path in the presence of the forces applied by the target, the cable moves around the connection point in a forward and reverse manner, which is in line with the expectation from the physics of the system.

Important criteria in control system design are the amount of control efforts and saturation of actuators in achieving control goals. Since NTAV is an agile high-speed robot equipped with strong rotors, it is expected that it can provide a minimum force equivalent to two to three times the total weight after capturing a flying object as shown in Fig. 15. This is also true for the attitude control of the quadrotor and the jet's servos based on Figs. 16 and 17. Considering the fact that the jet's servos are in free mode after the capturing phase, therefore, their control signals should be equal to zero in the transporting phase, Fig. 17.

In Figs. 18 and 19 and Table 4, a quantitative comparison is made between the tracking error and control effort of the designed controllers based on a number of performance metrics as [44].

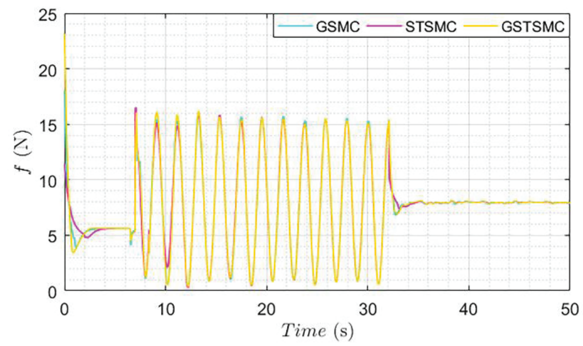

Fig. 15. Control input *f*.

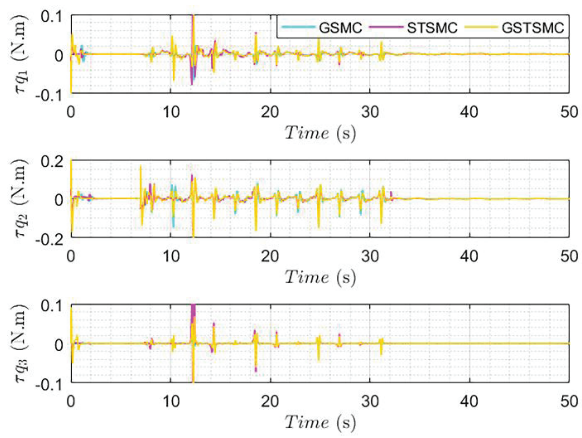

Fig. 16. Attitude control inputs of quadrotor.

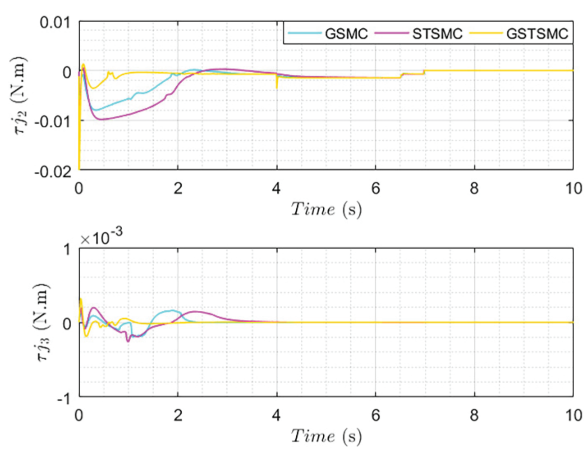

Fig. 17. Attitude control inputs of jet.

(1) The sum of integral absolute error (IAE): $\int |e_x| dt + \cdots + \int |e_\gamma| dt$.
(2) The sum of integral square error (ISE): $\int e_x^2 dt + \cdots + \int e_\gamma^2 dt$.
(3) The sum of integral absolute control input (IACI): $\int |u_1| dt + \cdots + \int |u_6| dt$.

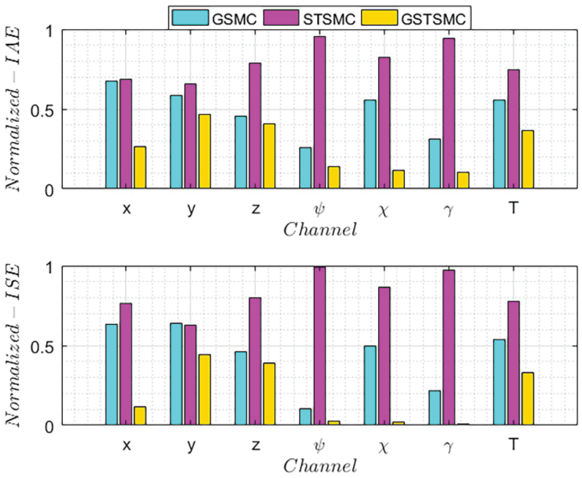

Fig. 18. Comparison based on tracking error.

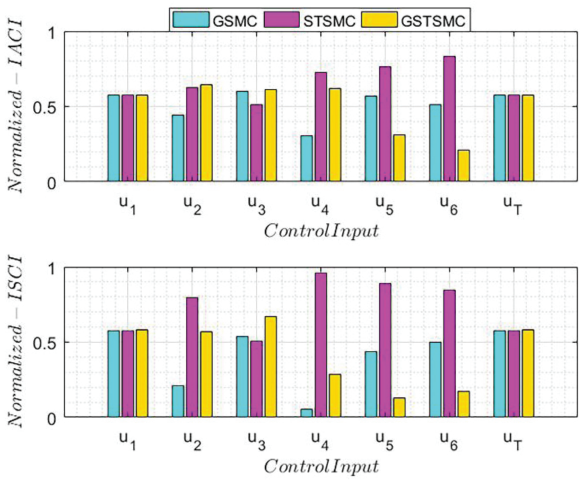

Fig. 19. Comparison based on control effort.

(4) The sum of integral square control input (ISCI): $\int u_1^2 dt + \cdots + \int u_6^2 dt$.

The letter T in Table 4 and the bar graphs denote "Total".

According to the bar charts 18 and 19 and Table 4, it can be inferred that via applying GSTSMC, trajectory tracking is realized with the higher speed and by far lower tracking errors in all channels with approximately the same control effort as the other two controllers which is an impressive advantage. In this regard, the tracking error of STSMC is considerably more than generalized algorithms when the precise estimate of target's mass is provided. In this condition, it can be said the SMC plus linear stabilizing term has a better tracking performance compared with standard STSMC without expending more control effort.

So far, it has been assumed that the state variables are accurately and ideally measured and provided to the controllers. In order to investigate the effect of measurement noise on the efficiency and consistency of the control systems, it is assumed that all measured state variables are affected by noise according to Fig. 20. The simulation results in this condition are depicted in Figs. 21–23.

Based on Fig. 21, the tracking performance of the controllers in the presence of measurement noise is favorable and the translational errors (e_x, e_y, e_z) have been bounded to (0.043, 0.015, 0.0075), (0.020, 0.023, 0.010) and (0.013, 0.015, 0.008) via GSMC, STSMC and GSTSMC, respectively. However, the range of variations of the vehicle's attitude states is increased, Fig. 22. In this respect, GSTSMC has the least range of variation that indicates the highest consistency of this controller in comparison with the other two algorithms in the face of measurement noise. On the other hand, although the tracking goal is fulfilled, in addition to high chattering, the amplitude of the control signals is increased, as illustrated in Fig. 23. In this condition, the values

Table 4. Quantitative comparison of the designed controllers based on tracking error and control effort.

Criterion	GSMC	STSMC	GSTSMC	Criterion	GSMC	STSMC	GSTSMC
IAE−x	• 5.3186	• 5.4131	• 2.1097	IACI−u_1	385.3341	385.5476	• 386.2748
IAE−y	3.3538	3.7597	2.6507	IACI−u_2	0.1337	0.1890	0.1944
IAE−z	5.4916	9.5213	4.9425	IACI−u_3	0.5355	0.4566	0.5496
IAE−ψ	0.0202	0.0743	0.0108	IACI−u_4	0.0482	0.1140	0.0969
IAE−χ	0.6593	0.9722	0.1342	IACI−u_5	0.0145	0.0195	0.0080
IAE−γ	0.0611	0.1849	0.0198	IACI−u_6	0.000196	0.000317	0.000079
IAE−T	14.9047	19.9255	9.8678	IACI−T	386.0662	386.3270	387.1238
ISE−x	5.4068	6.5432	0.9813	ISCI−u_1	3692.0754	3665.0039	3733.9713
ISE−y	3.5761	3.5136	2.4637	ISCI−u_2	0.0018	0.0067	0.0048
ISE−z	9.7978	17.0704	8.3015	ISCI−u_3	0.0341	0.0321	0.0426
ISE−ψ	0.000026	0.000241	0.000007	ISCI−u_4	0.0006	0.0108	0.0032
ISE−χ	0.2312	0.4016	0.0104	ISCI−u_5	0.0000640	0.0001303	0.0000187
ISE−γ	0.0031	0.0137	0.0001	ISCI−u_6	0.000000024	0.000000040	0.000000008
ISE−T	19.0150	27.5428	11.7569	ISCI−T	3692.1120	3665.0537	3734.0220

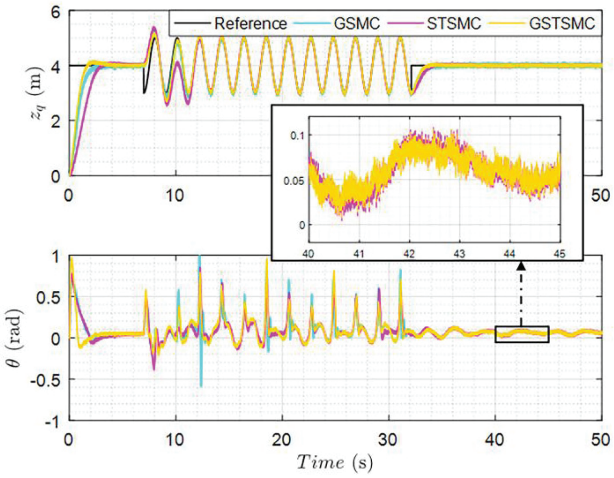

Fig. 20. Noisy state variables.

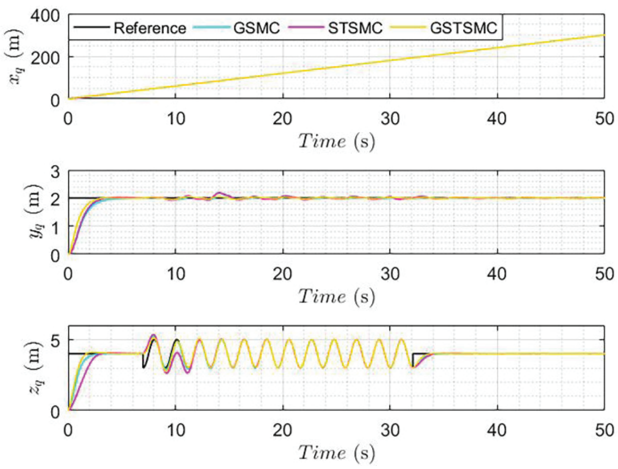

Fig. 21. Time response of x_q, y_q and z_q.

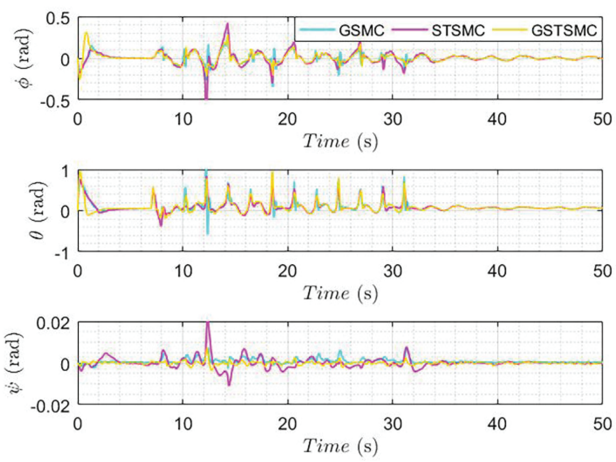

Fig. 22. Time response of ϕ, θ and ψ.

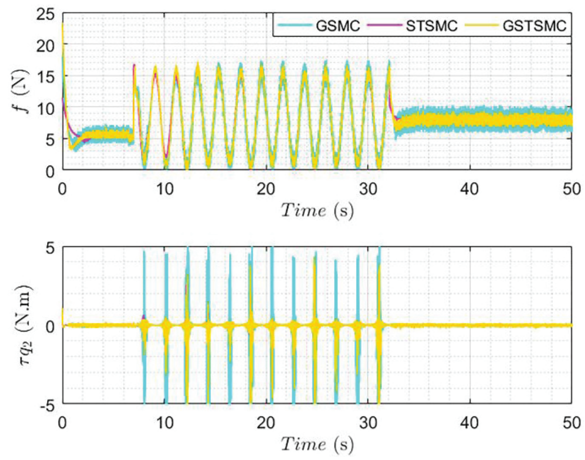

Fig. 23. Control inputs in the presence of noise.

of the total IACI and ISCI for (GSMC, STSMC, GSTSMC) have risen to $(396.1594, 390.0188, 393.4349)$ and $(3733.5920, 3671.6289, 3746.1418)$, respectively, which is higher than the corresponding values in Table 4. This issue in addition to depreciation, can lead to the saturation of actuators in real conditions, which is not desirable.

In Figs. 24 and 25, a quantitative comparison is made based on the normalized IAE and IACI. The general pattern of the graphs is similar to the corresponding ones in Figs. 18 and 19. The bar graphs show that GSTSMC has by

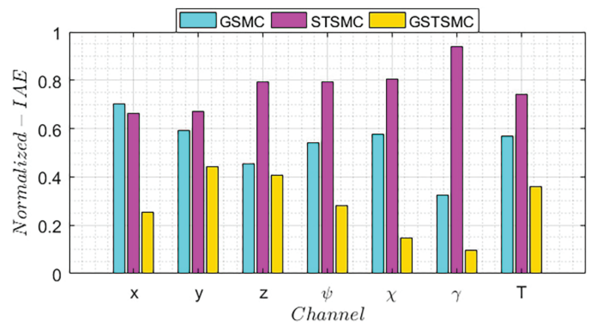

Fig. 24. Comparison based on tracking error.

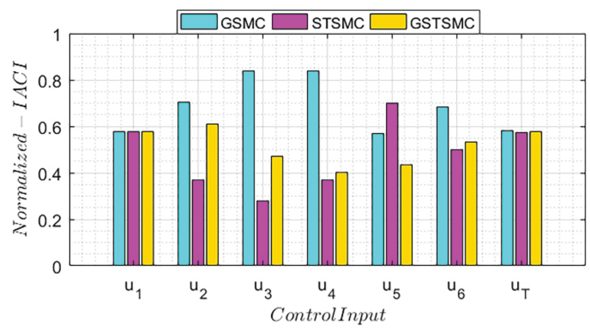

Fig. 25. Comparison based on control effort.

far the best performance in terms of tracking error and speed, but the amount of control effort via applying STSMC is slightly less than the two generalized first and second-order algorithms.

5. Conclusion

In this research, an accurate hybrid mathematical model of an NTAV to capture flying objects with high reliability is extracted and a model-based control strategy is depicted. In this regard, due to the presence of intense time-varying disturbances and parametric and nonparametric uncertainties, a generalized robust nonlinear controller equipped with a high performance estimator is designed for the system that by the accurate estimation of the target's inertia, the goals of stabilization and precise tracking, especially at the moment of capturing an oscillatory flying object, are fulfilled. In this regard, the performance of the designed controller with respect to GSMC and STSMC is evaluated through simulation. According to the simulation results and scrutinizing the time response of the system's state variables and control inputs, especially while capturing flying objects, it can be concluded that the presented hybrid model is completely valid and can satisfy the goals of the multi-step mission. In this regard, without considering the target's mass in control system, GSTSMC has by far better tracking performance and in addition to higher convergence rate, it has been able to limit the steady state error to 0.03 m in vertical motion. On the other hand, with accurate estimation of the target's mass, although GSTSMC has still the best performance in terms of IAE and ISE in all translational and attitudinal channels, the efficiency of other algorithms, especially GSMC, has been greatly improved and in addition to reducing the error bound to nearly zero, the IAE in the vertical motion is only 11% higher than the same value obtained via GSTSMC, which can be attributed to the higher convergence rate of generalized second order algorithm. It shows that by an accurate estimation of the target's mass, desirable time response can be achieved through GSMC and STSMC which has a less computational cost compared with GSTSMC.

Evaluating the efficiency of the controllers in the presence of measurement noise reveals that although their tracking performance is satisfactory, noisy feedback variables have a destructive effect on the control system and lead to highly oscillatory control inputs with a high range of variations. This issue shows that via applying an efficient filter and observer, the effect of noise on measured state variables should be reduced and if possible eliminated. This subject along with equipping the NTAV with an efficient guidance law and visual-based sensors, which is inevitable for capturing a flying object from practical point of view, and also considering control constraints, such as saturation, are the topics for future research.

Funding

This research received no specific grant from any funding agency in the public, commercial, or not-for-profit sectors.

Declaration of Competing Interests

The authors declare that there is no conflict of interest.

Appendix A.

The transformation matrices of jet body coordinate system with respect to the quadrotor body coordinate system and cable body coordinate system with respect to inertial coordinate system are equal to

$$[T]^{JQ} = \begin{bmatrix} S_\chi & 0 & -C_\chi \\ 0 & 1 & 0 \\ C_\chi & 0 & S_\chi \end{bmatrix} \begin{bmatrix} C_\gamma & S_\gamma & 0 \\ -S_\gamma & C_\gamma & 0 \\ 0 & 0 & 1 \end{bmatrix}, \tag{A.1}$$

$$[T]^{CI} = \begin{bmatrix} C_\beta & 0 & -S_\beta \\ 0 & 1 & 0 \\ S_\beta & 0 & C_\beta \end{bmatrix} \begin{bmatrix} C_\lambda & S_\lambda & 0 \\ -S_\lambda & C_\lambda & 0 \\ 0 & 0 & 1 \end{bmatrix}, \tag{A.2}$$

and the angular velocities of jet body frame with respect to the quadrotor body frame and cable body frame with respect to inertial frame are obtained as

$$[\omega^{JQ}]^J = \begin{bmatrix} 0 \\ -\dot{\chi} \\ 0 \end{bmatrix} + \begin{bmatrix} S_\chi & 0 & -C_\chi \\ 0 & 1 & 0 \\ C_\chi & 0 & S_\chi \end{bmatrix} \begin{bmatrix} 0 \\ 0 \\ \dot{\gamma} \end{bmatrix} = \begin{bmatrix} -\dot{\gamma} C_\chi \\ -\dot{\chi} \\ \dot{\gamma} S_\chi \end{bmatrix}, \tag{A.3}$$

$$[\omega^{CI}]^C = \begin{bmatrix} 0 \\ \dot{\beta} \\ 0 \end{bmatrix} + \begin{bmatrix} C_\beta & 0 & -S_\beta \\ 0 & 1 & 0 \\ S_\beta & 0 & C_\beta \end{bmatrix} \begin{bmatrix} 0 \\ 0 \\ \dot{\lambda} \end{bmatrix} = \begin{bmatrix} -\dot{\lambda} S_\beta \\ \dot{\beta} \\ \dot{\lambda} C_\beta \end{bmatrix}. \tag{A.4}$$

As mentioned in the text, the jet attitude angles χ and γ are calculated with respect to the inertial coordinate system in the transporting phase. In this respect, the transformation matrix (A.1) and angular velocity (A.3) are changed to $[T]^{JI}$ and $[\omega^{JI}]^{J}$, respectively.

Appendix B.

Considering the fact that the attitude dynamics of the jet is affected by the attitude dynamics of the quadrotor in the pursuit phase, the assumption of compatibility of the jet's connection point to the c.g of the vehicle does not decouple translational and rotational dynamics of the Flying System completely in this phase. But due to the small inertia of the jet-net-cable set with respect to the quadrotor, it tries to decouple these two dynamics by removing attitude terms from the translational one and vice versa. In this respect, the control model is obtained as follows:

$$\begin{bmatrix} \boldsymbol{H}_{T_{3\times3}} & \mathbf{0}_{3\times5} \\ \mathbf{0}_{5\times3} & \boldsymbol{H}_{A_{5\times5}} \end{bmatrix} \begin{bmatrix} \ddot{\boldsymbol{X}}_T \\ \ddot{\boldsymbol{X}}_A \end{bmatrix} + \begin{bmatrix} \boldsymbol{C}_{T_{3\times3}} & \mathbf{0}_{3\times5} \\ \mathbf{0}_{5\times3} & \boldsymbol{C}_{A_{5\times5}} \end{bmatrix} \begin{bmatrix} \dot{\boldsymbol{X}}_T \\ \dot{\boldsymbol{X}}_A \end{bmatrix} + \begin{bmatrix} \boldsymbol{G}_T \\ \boldsymbol{G}_A \end{bmatrix} = \begin{bmatrix} \boldsymbol{I}_{3\times3} & \mathbf{0}_{3\times5} \\ \mathbf{0}_{5\times3} & \boldsymbol{W}_{5\times5} \end{bmatrix} \begin{bmatrix} \boldsymbol{u}_T \\ \boldsymbol{u}_A \end{bmatrix} + \begin{bmatrix} \boldsymbol{f}_{a_T} \\ \mathbf{0} \end{bmatrix} + \begin{bmatrix} \mathbf{0} \\ \boldsymbol{\tau}_{gyr} \end{bmatrix}, \quad \text{(B.1)}$$

where $\boldsymbol{H}_i$, $\boldsymbol{C}_i$ and $\boldsymbol{G}_i$ are the inertial and Coriolis-centripetal matrices and gravity vector corresponding to each of the translational (T) and attitude (A) dynamics, respectively. In this regard, $\boldsymbol{u}_i$, $\boldsymbol{f}_{a_T}$ and $\boldsymbol{\tau}_{gyr}$ indicate the vectors of control inputs, aerodynamic drag forces and gyroscopic moments, respectively.

Based on this simplification, the direct dynamic model of translational dynamics is obtained similar to the corresponding one in the transporting phase. Considering $\boldsymbol{X}_A = [\phi\ \theta\ \psi\ \chi\ \gamma]^T$ and $\boldsymbol{u}_A = [\tau_{q_1}\ \tau_{q_2}\ \tau_{q_3}\ \tau_{j_2}\ \tau_{j_3}]^T$, the elements of direct attitude dynamics of NTAV in the pursuit phase based on expressed control strategy are obtained as

$$\begin{cases} \widehat{\boldsymbol{F}}(\boldsymbol{X}_A) = \boldsymbol{H}_A^{-1}(-\boldsymbol{C}_A\dot{\boldsymbol{X}}_A - \boldsymbol{G}_A + \boldsymbol{\tau}_{gyr}), \\ \widehat{\boldsymbol{G}}(\boldsymbol{X}_A) = \boldsymbol{H}_A^{-1}\boldsymbol{W}, \end{cases} \quad \text{(B.2)}$$

where $\boldsymbol{H}_A$ and $\boldsymbol{C}_A$ and $\boldsymbol{G}_A$ are extracted from the system's mathematical model expressed in Sec. 2.1 and $\boldsymbol{\tau}_{gyr}$ and $\boldsymbol{W}$ are obtained as follows:

$$\boldsymbol{\tau}_{gyr} = \boldsymbol{W}[\tau_{gyr_1}\quad \tau_{gyr_2}\quad 0\quad 0\quad 0]^T, \quad \text{(B.3)}$$

$$\boldsymbol{W} = \begin{bmatrix} 1 & 0 & 0 & 0 & 0 \\ 0 & C_\phi & -S_\phi & 0 & 0 \\ -S_\theta & S_\phi C_\theta & C_\phi C_\theta & 0 & 0 \\ 0 & 0 & 0 & 1 & 0 \\ 0 & 0 & 0 & 0 & 1 \end{bmatrix}. \quad \text{(B.4)}$$

The relations of $\boldsymbol{\tau}_{gyr_1}$ and $\boldsymbol{\tau}_{gyr_2}$ in (B.3) are shown in Table 2.

ORCID

Mirshams Baha https://orcid.org/0000-0002-5087-0501
Fariborz Saghafi https://orcid.org/0000-0003-0900-0229

References

[1] T. Baca, P. Stepan, V. Spurny, D. Hert, R. Penicka, M. Saska, J. Thomas, G. Loianno and V. Kumar, Autonomous landing on a moving vehicle with an unmanned aerial vehicle, *J. Field Robot.* **36**(5) (2019) 874–891.
[2] S. H. Arul and D. Manocha, Dcad: Decentralized collision avoidance with dynamics constraints for agile quadrotor swarms, *IEEE Robot. Autom. Lett.* **5**(2) (2020) 1191–1198.
[3] X. Jin and Z. Hu, Adaptive cooperative load transportation by a team of quadrotors with multiple constraint requirements, *IEEE Trans. Intell. Transp. Syst.* **24**(1) (2022) 801–814.
[4] C. M. Pappalardo, M. Del Giudice, E. B. Oliva, L. Stieven and A. Naddeo, Computer-aided design, multibody dynamic modeling, and motion control analysis of a quadcopter system for delivery applications, *Machines* **11**(4) (2023) 464.
[5] G. Roggi, G. Gozzini, D. Invernizzi and M. Lovera, Vision-based air-to-air autonomous landing of underactuated vtol uavs, *IEEE/ASME Trans. Mechatronics* **29**(3) (2023) 2338–2349.
[6] A. Mohiuddin, T. Tarek, Y. Zweiri and D. Gan, A survey of single and multi-UAV aerial manipulation, *Unmanned Syst.* **8**(2) (2020) 119–147.
[7] J. Meng, J. Buzzatto, Y. Liu and M. Liarokapis, On aerial robots with grasping and perching capabilities: A comprehensive review, *Front. Robot. AI* **8** (2022) 739173.
[8] D. Mellinger, M. Shomin, N. Michael and V. Kumar, Cooperative grasping and transport using multiple quadrotors, in *Distributed Autonomous Robotic Systems: The 10th International Symposium* (Springer, Berlin, Heidelberg, 2013), pp. 545–558.
[9] S. Kim, H. Seo, J. Shin and H. J. Kim, Cooperative aerial manipulation using multirotors with multi-dof robotic arms, *IEEE/ASME Trans. Mechatronics* **23**(2) (2018) 702–713.
[10] A. Khalifa and M. Fanni, Experimental implementation of a new non-redundant 6-DOF quadrotor manipulation system, *ISA Trans.* **104** (2020) 345–355.
[11] A. Suarez, M. Perez, G. Heredia and A. Ollero, Cartesian aerial manipulator with compliant arm, *Appl. Sci.* **11**(3) (2021) 1001.
[12] S. A. Emami and A. Banazadeh, Simultaneous trajectory tracking and aerial manipulation using a multi-stage model predictive control, *Aerosp. Sci. Techno.* **112** (2021) 106573.
[13] P. Yang, H. Wang, Z. Liu, Z. Dong and L. Zhang, Development of an anthropomorphic and dexterous dual-arm system for aerial cooperative bimanual manipulation, *Machines* **10**(4) (2022) 273.
[14] J. Thomas, J. Polin, K. Sreenath and V. Kumar, Avian-inspired grasping for quadrotor micro UAVs, in *Int. Design Engineering Technical Conferences and Computers and Information in Engineering Conference*, 55935 (American Society of Mechanical Engineers, 2013), p. V06AT07A014.
[15] J. Thomas, G. Loianno, K. Sreenath and V. Kumar, Toward image based visual servoing for aerial grasping and perching, in *2014 IEEE Int. Conf. on Robotics and Automation (ICRA)*, IEEE, 2014, pp. 2113–2118.
[16] X. Song and S. Hu, Hierarchy-based adaptive generalized predictive control for aerial grasping of a quadrotor manipulator, *J. Shanghai Jiaotong Univ. (Science)* **24** (2019) 451–458.
[17] W. Stewart, E. Ajanic, M. Müller and D. Floreano, How to swoop and grasp like a bird with a passive claw for a high-speed grasping, *IEEE/ASME Transactions on Mechatronics.* **27**(5) (2022) 3527–3535.

[18] J. Fishman and L. Carlone, Control and trajectory optimization for soft aerial manipulation, in *2021 IEEE Aerospace Conference* (50100), IEEE, 2021, pp. 1–17.

[19] A. X. Appius, E. Bauer, M. Blöchlinger, A. Kalra, R. Oberson, A. Raayatsanati, P. Strauch, S. Suresh, M. von Salis and R. K. Katzschmann, Raptor: Rapid aerial pickup and transport of objects by robots, in *2022 IEEE/RSJ International Conference on Intelligent Robots and Systems (IROS)* (IEEE, 2022), pp. 349–355.

[20] Z. W. Lee, W. H. Chin and H. W. Ho, Air-to-air micro air vehicle interceptor with an embedded mechanism and deep learning, *Aerosp. Sci. Technol.* **135** (2023) 108192.

[21] Z. Y. Lv, Y. Wu and W. Rui, Nonlinear motion control for a quadrotor transporting a cable-suspended payload, *IEEE Trans. Veh. Technol.* **69**(8) (2020) 8192–8206.

[22] D. Hashemi and H. Heidari, Trajectory planning of quadrotor UAV with maximum payload and minimum oscillation of suspended load using optimal control, *J. Intell. Robot Sys.* **100**(3–4) (2020) 1369–1381.

[23] P. Abeshtan and F. Saghafi, An innovative integrated path planning and trajectory tracking framework for a quadrotor slung load system in an urban environment, *Proc. Inst. Mech. Eng. Part G: J. Aerosp. Eng.* **237**(13) (2023) 2918–2938.

[24] P. H. Zipfel, Modeling and simulation of aerospace vehicle dynamics, American Institute of Aeronautics and Astronautics (AIAA), 3rd edn. (2014).

[25] E. L. de Angelis, Stability analysis of a multirotor vehicle hovering condition, *Aerosp. Sci. Technol.* **72** (2018) 248–255.

[26] https://www.youtube.com/watch?v=nlRkwuAcUd4.

[27] P. J. Cruz and R. Fierro, Cable-suspended load lifting by a quadrotor UAV: Hybrid model, trajectory generation, and control, *Auton. Robots* **41** (2017) 1629–1643.

[28] M. Baha and F. Saghafi, 3-D dynamic modeling and simulation of a quadrotor transporting cable-suspended payload generating stochastic forces, *Modares Mech. Eng.* **22**(7) (2022) 429–439.

[29] M. A. Vaz, M. H. Patel and J. A. Witz, Three-dimensional transient behavior of towed marine cables, *J. Ship Res.* **41**(01) (1997) 45–56.

[30] M. Rezaei, "3-D simulation of aerial towed system," MSc Thesis, Sharif University of Technology (2003) (In Persian).

[31] C. Powers, D. Mellinger and V. Kumar, Quadrotor kinematics and dynamics. in *Handbook of Unmanned Aerial Vehicles*, eds. K. Valavanis and G. Vachtsevanos (Springer, Dordrecht, 2015), pp. 307–28.

[32] Y. Niño, K. Vidal, A. Tamburrino, L. Zamorano, J. F. Beltrán, G. Estay and A. Muñoz, Normal and tangential drag forces of nylon nets, clean and with fouling, in fish farming, an experimental study, *Water* **12**(8) (2020) 2238.

[33] G. Hattenberger, M. Bronz and J. P. Condomines, Evaluation of drag coefficient for a quadrotor model, *Int. J. Micro Air Vehicles.* **15** (2023) 17568293221148378.

[34] S. Mobayen, An adaptive chattering-free PID sliding mode control based on dynamic sliding manifolds for a class of uncertain nonlinear systems, *Nonlinear Dynam.* **82**(1–2) (2015) 53–60.

[35] Y. Xie, X. Zhang, L. Jiang, J. Meng, G. Li and S. Wang, Sliding-mode disturbance observer-based control for fractional-order system with unknown disturbances, *Unmanned Syst.* **8**(03) (2020) 193–202.

[36] X. Wu, B. Xiao and Y. Qu, Modeling and sliding mode-based attitude tracking control of a quadrotor UAV with time-varying mass, *ISA Trans.* **124** (2022) 436–443.

[37] M. Zeinali and L. Notash, Adaptive sliding mode control with uncertainty estimator for robot manipulators, *Mech. Mach. Theory* **45**(1) (2010) 80–90.

[38] J. A. Moreno, A linear framework for the robust stability analysis of a generalized super-twisting algorithm, in *2009 6th Int. Conf. on Electrical Engineering, Computing Science and Automatic Control (CCE)*, IEEE, 2009, pp. 1–6.

[39] H. Yang, Y. Bai and Y. R. Chien, Generalized super-twisting sliding mode control of permanent magnet synchronous motor based on sinusoidal saturation function, *IEICE Electron. Express* **19**(9) (2022) 20220066.

[40] X. Lin, B. Zhang, S. Fang, R. Xu, S. Guo and J. Liu, Adaptive generalized super twisting sliding mode control for PMSMs with filtered high-gain observer, *ISA Trans.* **138** (2023) 639–649.

[41] Y. Shtessel, M. Taleb and F. Plestan, A novel adaptive-gain super-twisting sliding mode controller, *Methodol. Appl Autom.* **48**(5) (2012) 759–769.

[42] A. R. Babaei, M. Malekzadeh and D. Madhkhan, Adaptive super-twisting sliding mode control of 6-DOF nonlinear and uncertain air vehicle, *Aerosp. Sc. Technol*. **84** (2019) 361–374.

[43] K. J. Åström and B. Wittenmark, *Adaptive Control* (Courier Corporation, 2008).

[44] N. S. Özbek, M. Önkol and M. Efe, Feedback control strategies for quadrotor-type aerial robots: a survey, *Trans. Inst. Meas. Control* **38**(5) (2016) 529–554.

Mirshams Baha received his B.Sc. and M.Sc. in Mechanical Engineering (Applied Design) from the Islamic Azad University - Takestan Branch (TIAU) and M.Sc. in Aerospace Engineering (Flight Dynamics and Control) from the Sharif University of Technology (SUT) in 2010, 2014 and 2018, respectively. He is now a Ph.D. candidate in Flight Dynamics and Control at SUT. His research interests include Multibody Dynamics Modeling and Simulation, Flight Dynamics, Nonlinear Dynamics & Chaos, Nonlinear & Adaptive Control, Celestial Mechanics and Mathematics.

Fariborz Saghafi received his Ph.D. in Flight Dynamics from Cranfield University, UK, in 1996. He is currently Associate Professor in the Flight Dynamics and Control Group, Department of Aerospace Engineering, Sharif University of Technology. His interests include Flight Dynamics, Modeling and Simulation of Aerospace Systems, Aerial Robotics, Cooperative Missions, Rotorcraft, Simulator-Based Research and Education, Vision Aided Navigation and Guidance, and Aviation Industry.